Article

Delineating Groundwater Potential Zones in Hyper-Arid Regions Using the Applications of Remote Sensing and GIS Modeling in the Eastern Desert, Egypt

Hesham Morgan [1,*] , Hussien M. Hussien [2] , Ahmed Madani [1] and Tamer Nassar [1]

1   Department of Geology, Faculty of Science, Cairo University, Giza 12613, Egypt
2   Geology Department, Desert Research Center, El Mataryia, Cairo 11753, Egypt
*   Correspondence: hesham.hashem.geo@cu.edu.eg; Tel.: +20-1023994752

Abstract: The increasing demand for freshwater supplies and the effects of climate change in arid and hyper-arid regions are pushing governments to explore new water resources for food security assurance. Groundwater is one of the most valuable water resources in these regions, which are facing water scarcity due to climatic conditions and limited rainfall. In this manuscript, we provide an integrated approach of remote sensing, geographic information systems, and analytical hierarchical process (AHP) to identify the groundwater potential zone in the central Eastern Desert, Egypt. A knowledge-driven GIS-technique-based method for distinguishing groundwater potential zones used multi-criteria decision analysis and AHP. Ten factors influencing groundwater were considered in this study, including elevation, slope steepness, rainfall, drainage density, lineament density, the distance from major fractures, land use/land cover, lithology, soil type, and the distance from the channel network. Three classes of groundwater prospective zones were identified, namely good potential (3.5%), moderate potential (7.8%), and poor potential (88.6%) zones. Well data from the study area were used to cross-validate the results with 82.5% accuracy. During the last 8 years, the static water level of the Quaternary alluvium aquifer greatly decreased (14 m) due to excessive over pumping in the El-Dir area, with no recorded recharges reaching this site. Since 1997, there has been a noticeable decline in major rainfall storms as a result of climate change. The current study introduces a cost-effective multidisciplinary approach to exploring groundwater resources, especially in arid environments. Moreover, a significant modern recharge for shallow groundwater aquifers is taking place, even in hyper-arid conditions.

Keywords: remote sensing; weighted overlay model; analytical hierarchical process (ahp); thematic layers; climate change

1. Introduction

Groundwater is an important and vital source of freshwater supplies and sometimes a key issue in a country's socio-economic development, especially in places that fall within arid/hyper-arid belts [1,2]. About 2.5 billion people worldwide depend completely on groundwater to fulfill their basic water needs [3]. The demand for freshwater resources is expected to rise, with global water deficiency expected to reach 40 % by 2030 [4]. Because of the increased demand for freshwater in arid and hyper-arid regions, governments are looking for alternate water resources. Egypt is dependent on the Nile for 98.26% of its annual water demand [5]. The Grand Ethiopian Renaissance Dam has complicated the problem, and it may result in a major water shortage for the Nile River's downstream countries, whose populations are heavily reliant on the river's water [6]. Furthermore, Water resource demand has risen in recent decades as a result of population, economic, and agricultural growth.

Traditional methods for identifying, delineating, and mapping groundwater potential zones depend on expensive and time-consuming ground surveys using geological, geo-

physical, and hydrogeological tools [7–10]. Geospatial tools, on the other hand, are quick and inexpensive for producing and modeling useful data from a wide variety of geoscience fields [11–14]. The geographic information system (GIS) and remote sensing have proven to be extremely effective tools in groundwater exploration on their own. For groundwater potential zone identification, several GIS techniques have been used. They are beneficial in fuzzy logic analysis [15], analytical hierarchical processes (AHPs) [16], multi-influence factor analysis [7], etc. Satellite data with moderate and high spatial resolutions provide indirect information on groundwater storage. A small to great amount of information about indirect parameters can be gained from these satellites [17,18].

Several writers have published articles about employing remote sensing and GIS approaches to produce groundwater potential zones (Table 1). According to [19], the significant factors influencing groundwater accumulation are classified into three categories, including (a) major water supplies, including the water source and the possible contribution to the groundwater (e.g., rainfall and the distance from the channel network); (b) possible infiltration pathways (e.g., lithology (geology), lineament density, the distance from a major fracture, soil type, and land use/land cover); and (c) opportunity, which refers to the amount of time available to infiltrate the water supply; (e.g., elevation, slope steepness, and drainage density).

The main problems in the study area are the arid condition and water scarcity, which require a good plan for groundwater exploration and the sustainable management of water resources. The mapping of groundwater potentiality is highlighted in the early planning. This study uses the AHP model in a GIS environment to identify groundwater potential zones. The results of this study will have a significant influence on the early planning of groundwater exploration since it could provide preliminarily accurate information on the best location to target to drill good potential groundwater wells. After that, the use of geophysical techniques is a later step to confirm the results of the model before starting the drilling process, especially in an arid location which has no groundwater information.

In this paper, a cost-effective multidisciplinary research approach comprises the integration of the geographic information system, satellite and well log datasets as well as thematic layers produced from ArcGIS and field data to identify groundwater potential zones (potentiality mapping) in dry wadies in arid environments. This approach was achieved through the following: (1) extracting suitable thematic layers; (2) integrating all thematic layers using the analytical hierarchical process (AHP) and initiating a groundwater potential map for the study area based on the extracted thematic layers; (3) validating the applied model using the measured static water level during field trips to estimate the accuracy of obtained results; and (4) carrying out a frequency analysis for the historical rainfall data over 39 years to understand the rainfall behavior and identify the return period of the average annual precipitation, which could affect the groundwater recharging of the shallow aquifers in the study area. Finally, this manuscript provides a cost-efficient research approach for potential aquifer mapping in arid and hyper-arid environments, which could be a replicable model used in similar places that have the same conditions as our study area.

Table 1. Summary of the literature review of the different features that are used to identify groundwater potential zones (GWPZ).

N	Literature Review (Factors)	El	SI	Rf	DD	LD	G	Gm	LU/LC	Vg	TPI	TWI	ND	MF	ST	STh	R	SPI	ASPR	SPS	WTF	WTD	SWB	AR	Aspect	D	M	RI	ED	GWQ	NGWR
1	[20]		×		×	×	×	×														×	×								
2	[21]		×		×	×	×	×	×															×							
3	[22]		×		×	×	×	×														×									
4	[23]	×	×		×	×	×	×	×																						
5	[24]		×	×	×	×	×		×																						
6	[25]		×		×	×		×	×						×							×									
7	[26]				×	×	×	×	×	×					×																
8	[11]	×	×			×						×		×	×																
9	[27]		×	×	×	×	×															×								×	×
10	[28]		×		×	×	×	×																							
11	[29]		×	×	×	×	×		×						×																
12	[30]	×	×		×	×	×																								
13	[31]		×		×	×	×	×							×													×			
14	[32]		×			×		×																							
15	[33]	×	×	×	×	×	×		×	×		×			×				×												
16	[18]		×	×	×	×	×		×																						
17	[34]		×	×	×		×	×	×						×						×										
18	[35]		×	×	×	×		×	×						×	×															
19	[36]		×		×	×	×	×	×						×																
20	[37]		×	×	×	×	×	×	×						×																
21	[38]	×	×	×	×	×	×	×	×						×																
22	[39]	×			×	×	×	×							×																
23	[40]		×		×	×	×	×	×																						
24	[41]	×	×	×	×		×	×	×	×					×								×								
25	[42]	×	×		×	×	×								×																
26	[43]	×	×				×	×															×								
27	[16]		×	×	×	×	×	×	×	×	×	×			×		×		×												
28	[44]		×	×	×	×	×	×	×						×																
29	[45]		×	×	×	×	×	×	×						×																
30	[46]	×	×	×	×	×	×		×	×			×		×									×	×						

Table 1. *Cont.*

N	Literature Review	El	Sl	Rf	DD	LD	G	Gm	LU/LC	Vg	TPI	TWI	ND	MF	ST	STh	R	SPI	ASPR	SPS	WTF	WTD	SWB	AR	Aspect	D	M	RI	ED	GWQ	NGWR
31	[47]		×	×	×	×				×		×	×	×																	
32	[48]		×	×	×	×	×	×	×						×				×	×											
33	[4]		×	×	×	×	×	×							×																
34	[49]	×	×	×	×	×	×	×	×																						
35	[50]		×		×	×	×								×	×															
36	[19]		×	×		×	×					×													×						
37	[51]			×	×	×	×	×	×																						
38	[52]	×	×	×			×		×						×					×		×									
39	[53]		×	×	×	×	×		×							×															
40	[54]	×	×	×	×	×	×																			×	×	×	×		
41	[55]		×		×	×	×	×							×																
42	[56]		×	×	×	×	×	×	×						×								×								
43	[57]	×	×	×	×	×	×	×		×		×			×																
44	[58]		×		×	×	×	×							×									×							
45	[59]	×	×		×	×	×		×					×	×																

El = Elevation, Sl = Slope, Rf = Rainfall, DD = Drainage Density, LD = Lineament Density, G = Geology, Gm = Geomorphology, LU/LC = Land Use/Land Cover, Vg = Vegetation (NDVI), TPI = Topographic Position Index, TWI = Topographic Wetness Index, ND = Node Density, MF = Major Faults, ST = Soil Type, STh = Soil Thickness, R = Roughness, SPI = Stream Power Index, ASPR = Available Space for Recharge, SPS = Sand Percentage in the Soil, WTF = Water Table Fluctuation, WTD = Water Table Depth, SWB = Surface Water Body, AR = Apparent Resistivity, D = Depressions, M = Morphometry, RI = Radar Intensity, ED = Earthquake Density, GWQ: Groundwater quality, NGWR: Net Groundwater Recharge potentiality.

2. Site Description

The study area is located in the Nile valley, east of the cities of Idfu and Esna (Figure 1a). It crosses through the center of the Eastern Desert in a NE–SW direction. Geographically, it is bounded by the longitudes 32°33' and 34°15' E and the latitudes 24°52' and 25°37' N. It has a wide surface area that reaches around 8000 Km². The area's relief ranges from + 1043 m at the upstream portion to +74 m in the downstream parts. The central Eastern Desert is classified as an arid to hyper-arid region with an annual mean precipitation of about 8 mm/year, while the maximum air temperature was 43.7 °C and the minimum air temperature recorded during the period from 1981 to 2019 was 3 °C [60]. Geomorphologically, the Eastern Desert is separated into four major morphologic units, including the Red Sea crystalline mountains, the southern Sandstone plateau, the northern dissected limestone plateaus, and the narrow coastal plain. According to [61], the study area is mostly located on the Nubia Sandstone's southern sandstone plateau (Figure 1a). On the regional scale, the study area can be divided into two distinct topographic zones. The first is rugged, with high relief, and is made up of basement rocks. The second zone has low relief and is made up of sedimentary rocks. This zone slopes gently westward towards the Nile River and rises further east more steeply towards the basement range. Wadi Abadi and its subbasins, (e.g., El Baramya, Um Tanduba, El Shaghab, and El Myah) are located to the south of the study area. Among the studied catchments, Wadi Abadi has the largest drainage network, which covers about 6700 km². It extends 200 Km to the east until reaches the Red Sea mountainous terrains. To the north of the Abadi basin, many Wadies dissect the area from the east to the west, including Nuzul, El-Shikh Ali, Domi, Salah Nasr, Al-Mafallis, Hilal, Abu-Almahamid, El-Shaykh Nagar, Salim Judah, El-sharwna El-keblya, El-sharwna El-baharya, Kelabya, El-sabil, El-Dir, and El-Foley (Figure 1b). These Wadies are mostly cut in the sandstone plateau and do not reach the basement terrains.
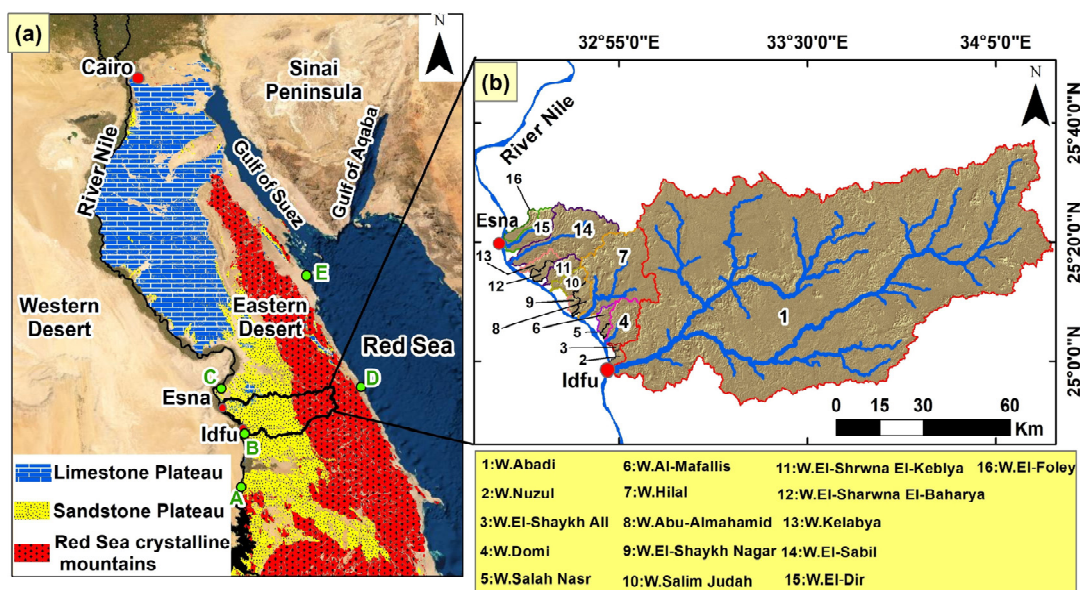
Figure 1. (**a**) General map of Egypt illustrating the geographic location of the study area associated with the nearest meteorological rain gauge stations (A: Aswan, B: Idfu, C: Luxor, D: Marsa Alam, and E: Hurghada); (**b**) close-up view of the different wadies dissecting the study area trending in an east–west direction.

3. Geological Setting

The East Esna–Idfu region is dominated by sedimentary succession ranging in age from Precambrian to recent. The exposed rock units are represented by a sedimentary succession underlain by Precambrian basement rocks. Taref Sandstone is a member of the Nubia Formation that overlies Precambrian rocks. Upper Cretaceous rocks lie non-

conformably on top of Precambrian basement rocks and are divided into four formations, including (from bottom to top) Nubia Sandstone, Quseir variegated shale, then Duwi and Dakhla formations [62]. The exposed sedimentary successions in the area are mainly marked by Upper Cretaceous rocks, and they mainly consist of Nubia Sandstone Fm. and Quseir Fm., covering the majority of the investigated area. The geological map shows the distribution of the rock units along Wadi Abadi (Figure 2).
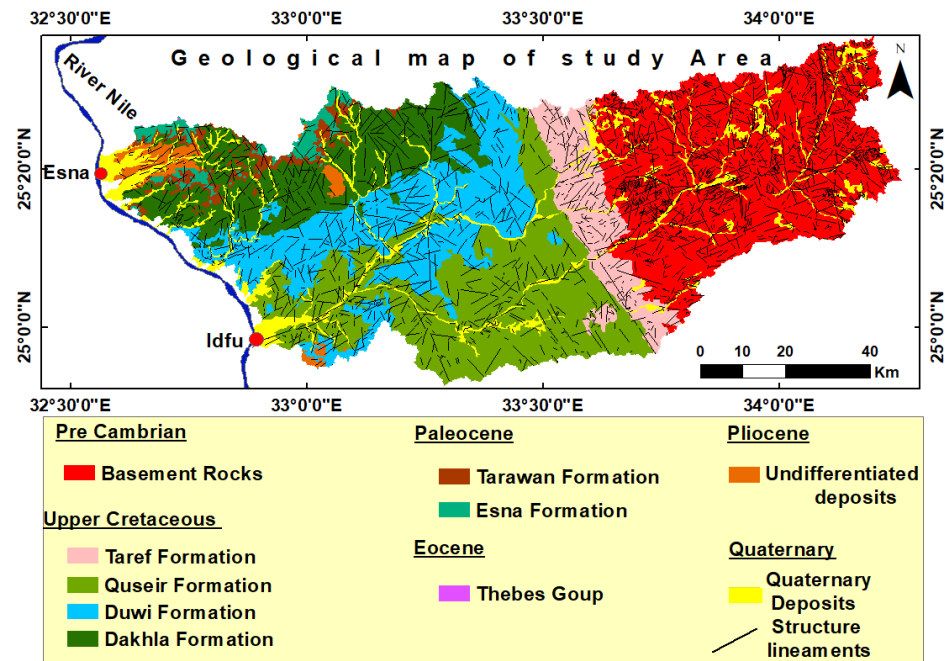
Figure 2. The distribution of various lithological units associated with extracted lineaments is shown on a geological map of the study area.

4. Methodology and Data

The current manuscript used several types of data to define the groundwater potential zones in the study area. In Figure 3, a flow chart illustrates the integrated approaches that were used to create the final map of groundwater potential zones during the current study. Four types of satellite remote sensing data were prepared for digital image processing, along with geologic maps [62] and fieldwork data, to create the groundwater characteristic layers needed to generate the potential groundwater map. The remote sensing data sources, included (1) a Landsat-8 Operational Land Imager (OLI) satellite image acquired on 1 July 2021 with a 30 m spatial resolution as well as a panchromatic band with a 15 m spatial resolution; (2) sentinel-2A satellite image data with a 10 m spatial resolution acquired on 29 June 2021; (3) Shuttle Radar Topography Mission (SRTM)s' Digital Elevation Model (DEM) of 1 arc-sec data with a 30 m resolution downloaded from [63]; and (4) The Modern-Era Retrospective Analysis for Research and Applications, version 2 (MERRA-2) Rainfall data of the last four decades over 39 years between January 1981 and December 2019 downloaded from [60]. MERRA-2 precipitation values were calibrated by the nearest meteorological rain gauge stations (Idfu, Aswan, Luxor, Hurghada, and Marsa Alam) and were obtained from the Egyptian meteorological authority. Principal component analyses (PCA), band ratio, and false color composite techniques were all used in this study to analyze spatial data. Lithology, lineament, major fractures, and soil type layers were all generated using these techniques. SRTM-DEM, sentinel-2A (verified by Google Earth), and MERRA-2 data were used to create elevation, slope steepness, drainage density, land use/land cover, distance from the channel network, and rainfall layers. To create these thematic layers, remote sensing and GIS techniques were used in different software environments, including ArcGIS 10.8 and Envi 5.1.
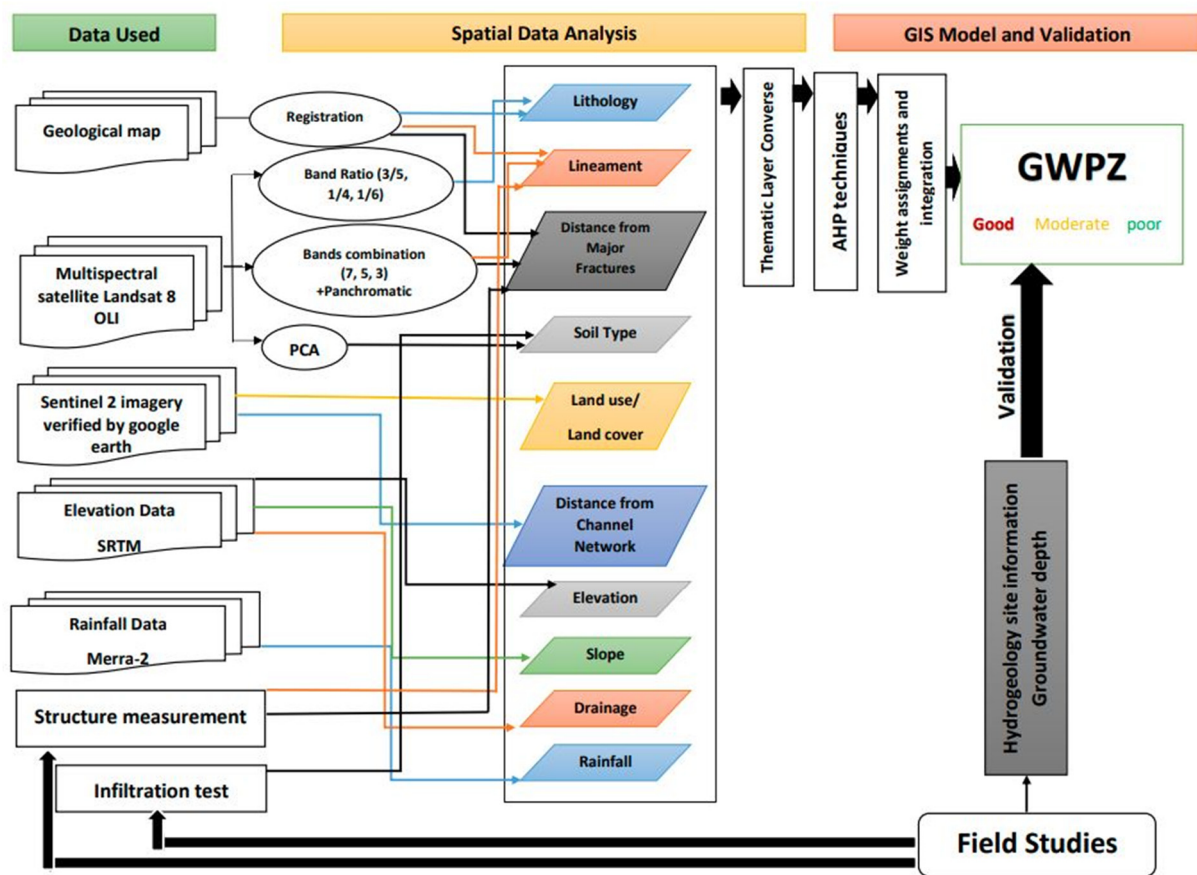
Figure 3. The flowchart illustrates the procedures involved in creating a groundwater potential zone map.

The most popular and well-known knowledge-driven GIS-technique-based method for distinguishing groundwater potential zones is a multi-criteria decision analysis using the analytical hierarchical process (AHP) [16,54]. This method helps in the integration of all thematic layers. This study included a total of ten different thematic layers. The ArcGIS 10.8 software was used to convert each continuous layer into a thematic layer with about five classes. Some guidelines were taken in the GIS model, including (1) based on their respective contributions to the occurrence of groundwater, assigning the following weight values (5, 4, 3, 2, or 1) to each class within the layer, with the greatest value going to high-potential areas; (2) ten groundwater parameters were integrated using an index overlay model; and (3) model validation using the static water level in the field. The weighting of these influencing factors was based on their reaction to the occurrence of groundwater and an expert viewpoint. A high weight parameter represents a layer with a large impact on groundwater potential, whereas a low weight parameter represents a layer with a minimal impact. The relative importance values of each parameter were assigned according to Saaty's scale (1–9). In addition, the weights were assigned based on a review of previous studies and field experience. According to Saaty's relative importance scale, a value of 9 indicates extreme importance, 8 indicates very strong importance, 7 indicates very strong to extreme importance, 6 indicates more than strong importance, 5 indicates strong importance, 4 indicates more than moderate importance, 3 indicates moderate importance, 2 indicates weak importance, and 1 indicates equal importance.

All of the thematic layers were compared to one another in a pair-wise comparison matrix (Table 2). The classes of each thematic layer ranking were awarded a score from 1 to 5 based on their proportionate effect on groundwater potentiality. Table 3 illustrates the criteria weight percent of the thematic layers associated with the rank and area of each class within every thematic layer. The following steps were used to calculate the consistency

ratio (CR): (1) the Eigen vector technique was used to calculate the principal Eigen value ($\acute{\Lambda}$) (Table 4), and (2) Equation (1) was used to obtain the consistency index (CI):

$$\acute{\Lambda}\mathrm{max} = 100/10 = 10$$

$$CI = \frac{L\mathrm{max} - \mathrm{n}}{n - 1}$$

(1)

where, n denotes the number of analyzed parameters.

$$Cl = (10 - 10)/(10 - 1) = 0$$

Table 2. Pair-wise comparison matrix of the ten thematic layers used in the current study.

Them	Assigned Weight	Elevation	Slope	Rainfall	Drainage Density	Lineament Density	Major Fractures	LULC	Lithology	Soil Type	Channel Network	Criteria Weight	Criteria Weight (Percent)
Elevation	3	3/3	3/3	3/5	3/4	3/6	3/3	3/2	3/7	3/8	3/3	0.068	6.8%
Slope	3	3/3	3/3	3/5	3/4	3/6	3/3	3/2	3/7	3/8	3/3	0.068	6.8%
Rainfall	5	5/3	5/3	5/5	5/4	5/6	5/3	5/2	5/7	5/8	5/3	0.113	11.4%
Drainage Density	4	4/3	4/3	4/5	4/4	4/6	4/3	4/2	4/7	4/8	4/3	0.091	9.1%
Lineament Density	6	6/3	6/3	6/5	6/4	6/6	6/3	6/2	6/7	6/8	6/3	0.136	13.6%
Major Fractures	3	3/3	3/3	3/5	3/4	3/6	3/3	3/2	3/7	3/8	3/3	0.068	6.8%
LULC	2	2/3	2/3	2/5	2/4	2/6	2/3	2/2	2/7	2/8	2/3	0.045	4.5%
Lithology	7	7/3	7/3	7/5	7/4	7/6	7/3	7/2	7/7	7/8	7/3	0.159	15.9%
Soil Type	8	8/3	8/3	8/5	8/4	8/6	8/3	8/2	8/7	8/8	8/3	0.181	18.2%
Channel Network	3	3/3	3/3	3/5	3/4	3/6	3/3	3/2	3/7	3/8	3/3	0.068	6.8%

Table 3. Factors influencing groundwater potential zones were classified associated with the area of each class.

Thematic Layer	Criteria Weight (%)	Class		Rank	Area km^2	Area (%)
(1) Elevation (DEM)	6.8	74–208 (ma.s.l)	(Very Low)	5	1122.4	14.1
		208–302 (ma.s.l)	(Low)	4	2903.2	36.4
		302–407 (ma.s.l)	(Moderate)	3	1768.6	22.1
		407–534 (ma.s.l)	(High)	2	1324.8	16.6
		534–1043 (ma.s.l)	(Very High)	1	866.5	10.9
(2) Slope Steepness (Degree)	6.8	0–3.6°	(Flat)	5	3299.9	41.3
		3.6–7.6°	(Gentle)	4	2601.6	32.6
		7.6–12.9°	(Moderate)	3	1308.9	16.4
		12.9–20°	(Steep)	2	598.1	7.5
		20–67.1°	(Very Steep)	1	177.1	2.2
(3) Drainage Density	9.1	1.112–1.171 (km/km^2)	(Very Low)	1	2586	32.4
		1.171–1.215 (km/km^2)	(Low)	2	2213.2	27.7
		1.215–1.259 (km/km^2)	(Moderate)	3	1840.6	23.1
		1.259–1.326 (km/km^2)	(High)	4	1200	15
		1.325–1.434 (km/km^2)	(Very High)	5	145.7	1.8

Table 3. *Cont.*

Thematic Layer	Criteria Weight (%)	Class		Rank	Area km^2	Area (%)
(4) Rainfall	11.4	2.33–3.46 (mm)	(Very Low)	1	4608.3	57.7
		3.46–4.15 (mm)	(Low)	2	1706.5	21.4
		4.15–5.08 (mm)	(Moderate)	3	912.8	11.4
		5.08–6.21 (mm)	(High)	4	415.3	5.2
		6.21–7.67 (mm)	(Very High)	5	342.6	4.3
(5) Lineament Density	13.6	0.27–0.47 (km/km^2)	(Very Low)	1	1784.7	22.3
		0.47–0.67 (km/km^2)	(Low)	2	3531.7	44.2
		0.67–0.87 (km/km^2)	(Moderate)	3	885	11.1
		0.87–1.08 (km/km^2)	(High)	4	1114.7	14
		1.08–1.28 (km/km^2)	(Very High)	5	669.3	8.4
(6) Distance from Major Fractures	6.8	<200 (m)	(Very Near)	5	212.2	2.7
		200–400 (m)	(Near)	4	231.5	2.9
		400–600 (m)	(Intermediate)	3	242	3
		600–800 (m)	(Far)	2	245.7	3
		800–1000 (m)	(Very Far)	1	148.7	3.1
(7) Lithology	15.9	Wadi Deposits (Quaternary) Different types of soil		5	810.3	10.1
		Taref Fm. (Paleozoic–Cret. "Turonian") Sandstone, fine to medium grained		4	526.1	6.6
		Issawia Fm. (Pliocene) Sandy clays, marls, shales, siliceous brecciated limestone, and conglomerates		3	114.6	1.4
		Duwi Fm. (Upper Cret. "Maastrichtian") Phosphate beds with black shale, marl, and oyster bed sandstone.		3	1339.6	16.8
		Tarwan Fm. (Paleocene) White Chalk and chalky limestone		3	164.4	2.1
		Thebes Group (Eocene) Chalk and chalky limestone bed rich in chert beds		3	3.6	0.1
		Quseir Fm. (Upper Cret. "Campanian") Varicolored shale, siltstone, and flaggy sandstone		2	1535.1	19.2
		Dakhla Fm. (Upper Cret. "Maastrichtian") Dark grey shallow marine marl and shale with intercalated limestone		2	1004.3	12.6
		Esna Fm. (Paleocene) Green to grey shales with gypsum veinlets altered with a marl bed		2	142.8	1.8
		Precambrian Basement rocks Igneous, metamorphic, and metasediments		1	2344.7	29.4
(8) Land Use/Land Cover	4.5	Wadi Deposit		5	685.7	8.6
		Natural desert grassland		5	29.7	0.4
		Cultivated Land		4	104	1.3
		Mining Area		2	106.7	1.3
		Barren Land		1	7059	88.4

Table 3. *Cont.*

Thematic Layer	Criteria Weight (%)	Class		Rank	Area km^2	Area (%)
(9) Soil Type (according to in-filtration rate)	18.2	Index 1 Infiltration capacity equilibrium = 13.8mm/min	(Very high)	5	218.8	2.7
		Index 2 Infiltration capacity equilibrium = 4.5mm/min	(High)	4	271.3	3.4
		Index 3 Infiltration capacity equilibrium = 2mm/min	(Moderate)	3	122.9	1.5
		Index 4 Infiltration capacity equilibrium = 0.53mm/min	(Low)	2	213.4	2.7
		Index 5 Not Soil "Rock"	(Very low)	1	7158.9	89.7
(10) Distance from Channel Network	6.8	0–600 (m)	(Very Near)	5	63.2	0.8
		601–1200 (m)	(Near)	4	38.6	0.5
		1201–1800 (m)	(Intermediate)	3	35.4	0.4
		1801–2400 (m)	(Far)	2	39	0.5
		2401–3000 (m)	(Very Far)	1	43.4	0.5

Table 4. The results of the consistency ratio.

Theme	Elevation	Slope	Rainfall	Drainage Density	Lineament Density	Major Fractures	LULC	Lithology	Soil Type	Channel Network	Weight Sum (Value)	λ
Elevation	0.068	0.068	0.068	0.068	0.068	0.068	0.068	0.068	0.068	0.068	0.682	10
Slope	0.068	0.068	0.068	0.068	0.068	0.068	0.068	0.068	0.068	0.068	0.682	10
Rainfall	0.114	0.114	0.114	0.114	0.114	0.114	0.114	0.114	0.114	0.114	1.136	10
Drainage Density	0.091	0.091	0.091	0.091	0.091	0.091	0.091	0.091	0.091	0.091	0.909	10
Lineament Density	0.136	0.136	0.136	0.136	0.136	0.136	0.136	0.136	0.136	0.136	1.364	10
Major Fractures	0.068	0.068	0.068	0.068	0.068	0.068	0.068	0.068	0.068	0.068	0.682	10
LULC	0.045	0.045	0.045	0.045	0.045	0.045	0.045	0.045	0.045	0.045	0.455	10
Lithology	0.159	0.159	0.159	0.159	0.159	0.159	0.159	0.159	0.159	0.159	1.591	10
Soil Type	0.182	0.182	0.182	0.182	0.182	0.182	0.182	0.182	0.182	0.182	1.818	10
Channel Network	0.068	0.068	0.068	0.068	0.068	0.068	0.068	0.068	0.068	0.068	0.682	10

The consistency ratio was defined using Equation (2), as follows:

$$CR = CI/RC \tag{2}$$

where RCI is the value of the random consistency index, whose values were taken from Saaty's standard (Table 5).

$$CR = 0/1.49 = 0$$

According to [64], a CR of 0.10 or less is appropriate for the analysis to continue. If the consistency value is larger than 0.10, the judgement should be revised to identify the sources of inconsistency and correct them. If the CR value is 0, it means that the pair-wise comparison has a perfect level of consistency. All ten thematic layers were combined in ArcGIS software using the weighted overlay analysis approach of Equation (3) to build a groundwater potential zone map for the research region [16,65].

	The Indices of Consistency of Randomly Generated Reciprocal Matrices [64]									
				The Matrix's Order						
N	**1**	**2**	**3**	**4**	**5**	**6**	**7**	**8**	**9**	**10**
RCI value *	0.00	0.00	0.58	0.90	1.12	1.24	1.32	1.41	1.45	1.49

* Random Consistency Index.

$$GWPZ = \sum_{i}^{n}(XA \times YB) \tag{3}$$

where, GWPZ refers to the groundwater potential zone, X denotes the weight of the thematic layers, and Y denotes the rank of the thematic layer class. The thematic map is represented by the A term (A = 1, 2, 3, . . . , X), and the thematic map classes are represented by the B term (B = 1, 2, 3, . . . , Y). The final groundwater potential zone map was divided into three groups: poor, moderate, and good.

Soil infiltration tests and sieve analyses were carried out in locations with different soil types that were selected based on the discrimination created by PCA technique to measure the infiltration capacity and calculate the hydraulic conductivity and specific yield using the Hazen method [66]. Sampling cores were made in Nubia Sandstone water-bearing rock at two different hand-dug wells located within Wadi Abadi to measure the actual porosity and permeability using a KA-210 gas permeameter and porosimeter and to identify the homogeneity of the major aquifer in the study area related to groundwater potentiality. A prediction of the rainfall return period for the future was made using the hydrologic engineering center (HEC) software to understand the behavior of rainfall and its impact on the aquifer potentiality in the study area. In order to undertake a frequency analysis and other statistical calculations, the HEC software supported a number of statistical software packages, such as HEC-DSSVUE and HEC-SSP2.2. HEC-DSSVUE allows users to edit and manipulate data in an HEC_DSS database file. HEC-SSP performs statistical analyses of hydrologic data.

5. Results and Discussion

5.1. Hydrogeological Condition

In the study area, three major aquifers have been identified; (a) an unconfined Quaternary alluvium aquifer; (b) a semi-confined Nubia Sandstone aquifer, which was detected in the middle and downstream of the Abadi basin; and (c) a Precambrian fractured basement aquifer. The inspection of well log data for three drilled wells illustrated that the Nubia Sandstone aquifer is the main water-bearing formation in the Abadi basin. This aquifer was tapped by 16 water points located at the main course of the wadi. Moreover, the fractured basement was tapped by six water points at the upstream portion of Wadi Abadi. Based on new drilling activity in the study area, two well log data points (well 8 and well 9) were obtained to illustrate the subsurface succession of the Nubia Sandstone aquifer, which is represented by the Taref Sandstone Formation. The cross-section (Figure 4) shows that the total penetrated thickness is about 360 m of fine to medium Sandstone with sandy shale and/or shale lenses. The two drilled wells fully penetrate the total thickness of the sandstone to the basement rocks at 425 m and 416 m at well 8 and well 9, respectively. The flow of groundwater generally runs from east to west. The depth to water ranges from 55 m to 44 m. The total dissolved salts in the three aquifers range from 1241 to 5826 mg/L. On the other hand, the Quaternary aquifer was detected in the Wadi El Dir area and was tapped by 11 water points. The depth to water ranged from 20 m to 63 m. The water level data of the three aquifers were used to validate the result of the tested model.
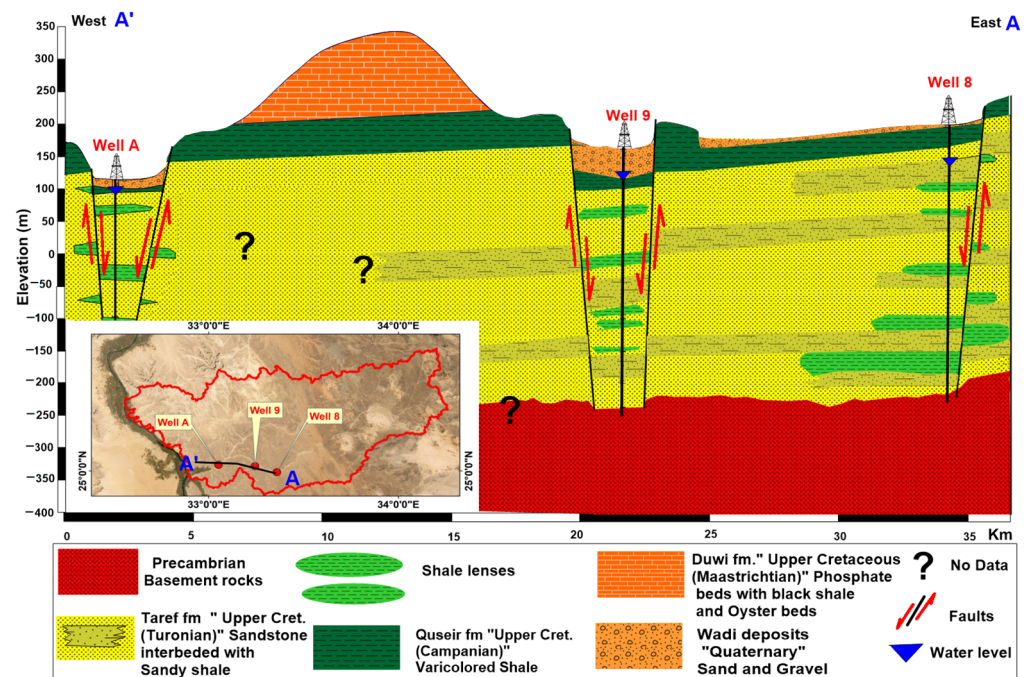
Figure 4. Schematic hydrogeological cross section (A–A') illustrates the subsurface lithological composition of the Nubia Sandstone aquifer at Wadi Abadi.

5.2. Preparation of Thematic Layers Influencing Groundwater Recharge

Remote sensing satellite data were utilized in this work to construct ten thematic factors (features) that govern groundwater potentiality. These features are elevation, slope steepness, drainage density, rainfall, lineament density, the distance from major fractures, lithology, land use/land cover, soil type, and the distance from the channel network. The paragraphs that follow explain in detail how each factor was generated from satellite data as well as the link to groundwater potentiality.

5.2.1. Elevation

Elevation has an indirect and inverse proportion to groundwater potentiality. As a result, greater elevations promote more recharge and assure groundwater supplies in a watershed's lowland parts. Mountainous areas typically contribute to recharging low-lying confined aquifers. [67,68]. Water tends to accumulate more at lower elevations than at higher elevations.

The digital elevation model (DEM) (Figure 5a) of the study area and SRTM-DEM data were used. The DEM is classified into five zones (Figure 5b) in the study area. The elevation ranges from 74 to 1043 m a.s.l. Very high elevations and the highest elevations are located in the eastern part, where basement rocks exist. Low-elevation zones encourage water accumulation and infiltration. The altitudes were reclassified into five groups depending on their ability to store and collect surface water. These classes included the following: very low (74–208), low (208–302), moderate (302–407), high (407–534), and very high (534–1043) elevations, covering around 14, 36, 22, 16.6, and 10.8 percent of the surface area, respectively. Very low and low elevations were given high weights. High and very high elevations were awarded low weights according to their relation to groundwater recharge.
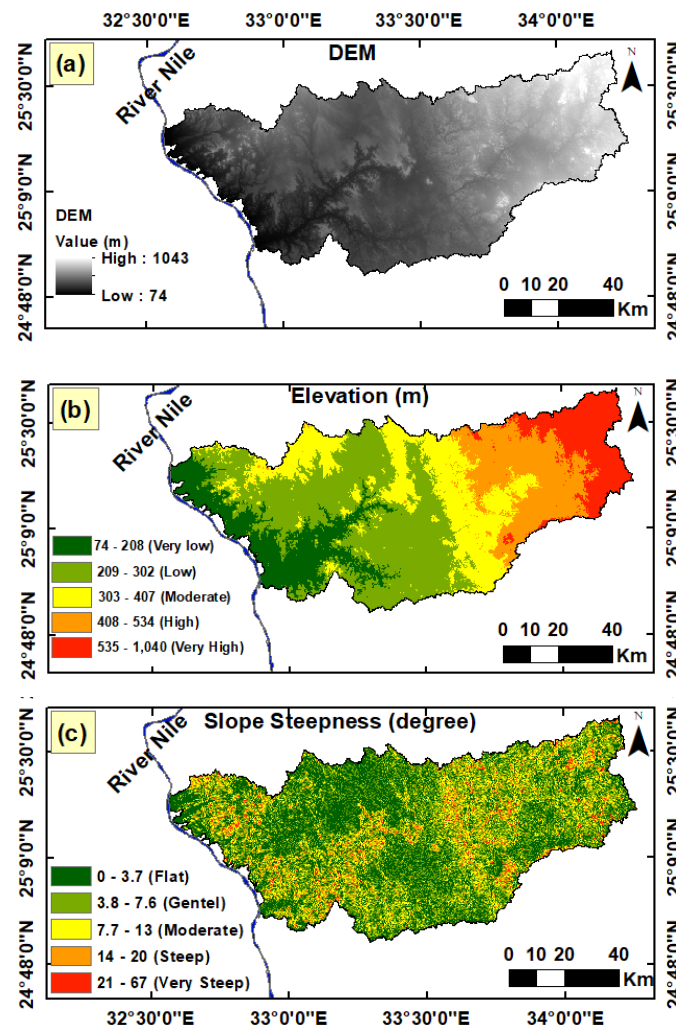
Figure 5. Digital elevation model and its derivatives. (**a**) SRTM-DEM data of the study area; (**b**) Elevation class map for the study area; (**c**) slope steepness map in degrees extracted from the digital elevation model.

5.2.2. Slope Steepness

Slope has a significant impact on the occurrence and movement of surface water and groundwater. Therefore, the slope can be a significant factor in runoff and infiltration. Groundwater prospecting areas were determined using the slope layer as an important feature [23]. Because the surface runoff resulting from precipitation flows quickly down to low-lying areas during rainfall storms, high slopes make a non-significant contribution to groundwater recharge.

The slope ranges from $0°$ to $67.14°$ (Figure 5c). From the slope map, the high slope steepness that ranges from 20.1 to 67.144 degrees is located around the main streams of the Abadi watershed, in the basement rocks, and in the northern area close to the limestone plateau. On the other hand, low-slope zones are preferable places for water accumulation and infiltration. The slope steepness values were classified into five categories based on their ability to store water. The slope steepness classes included the following: very gentle (0–3.6), gentle (3.6–7.6), moderate (7.6–12.9), steep (12.9–20), and very steep (20–67.1), covering approximately 41, 32.5, 16, 7, and 2 percent of the area, respectively. Very gentle and gentle slopes were given high weights. The steep and very steep slopes were awarded low weights since they do not give enough time for surface runoff to infiltrate and reach the shallow aquifer.

5.2.3. Density of Drainage Network

The drainage pattern and density provide excellent indicators of the hydrogeological properties of the land. Several factors influence the shape of the drainage pattern in a drainage basin, including the structure, climate, topography, soil type, geology, and vegetation [69,70]. The main patterns that characterize the study area are parallel and dendritic drainage patterns. In the upper and middle parts of the wadies, especially the largest one (Wadi Abadi), a dendritic drainage pattern can be seen, whereas a parallel drainage pattern characterizes the lower part near the outlets on the Nile River. The drainage networks in the investigated area (Figure 6a) were derived from SRTM-DEM data and processed in ArcGIS software using spatial analyst tools. The drainage density is the total length of streams per unit of area [71].
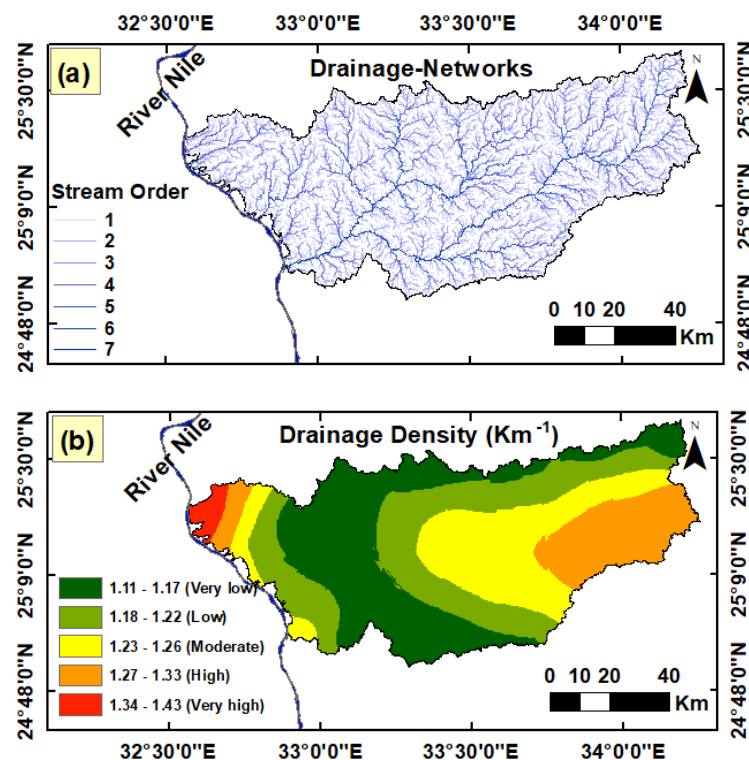
Figure 6. (**a**) Thematic layer of drainage networks of the study area extracted from DEM in the ArcGIS environment; (**b**) Drainage density map of the study area to illustrate the density distribution of the streams.

Several studies have found that the density of stream networks is inversely related to the rate of recharge processes [29,51], but other researchers have stated that the high drainage density reveals a high infiltration capability due to the highly dissected land surface [28,43,50]. In this research, we linked high-density locations to increased suitability for recharging and infiltration capacity. The average drainage density of the study area was 1097 km/km^2. The investigation and analysis of the drainage density map (Figure 6b) showed that high-drainage-density zone is located in the northwestern and eastern parts of the study area. Based on the availability of recharging and the infiltration capacity, the generated drainage density map was classified into five categories: very low (1.11–1.17 km/km^2), low (1.17–1.21 km/km^2), moderate (1.21–1.25 km/km^2), high (1.25–1.32 km/km^2), and very high (1.32–1.43 km/km^2), covering around 32, 27.7, 23, 15, and 1.8 percent of the studied surface area, respectively. Very high drainage density areas and high-drainage-density areas were given high weights. Low-drainage-density areas and very low drainage density areas were awarded low weights.

5.2.4. Precipitation (Rainfall Distribution)

In this study, The Modern-Era Retrospective Analysis for Research and Applications, version 2 (MERRA-2) for precipitation data were used to evaluate the amount of precipitation in the study area and to generate the rainfall layer used in the GIS model. Following the introduction of NOAA-18 in 2005, MERRA had no new satellite observation sources. MERRA-2, on the other hand, includes a slew of extra satellite observations both before and after this period. MERRA-2 is the latest atmospheric reanalysis of the modern satellite era produced by NASA's Global Modeling and Assimilation Office (GMAO) [72]. It is made available on a worldwide grid with a spatial resolution of 0.5° of latitude by 0.5° of longitude. MERRA-2 provides data beginning in 1981, so it is better than TRMM, which provides data beginning in 1997 because MERRA-2 has more historical data, and the MERRA-2 dataset produces more accuracy than the TRMM dataset [73,74].

To validate the MERRA-2 precipitation in the study area, two different methods were used in this research. First, the calibration of MERRA-2 with values from the nearest metrological rain gauge stations (Idfu, Aswan, Luxor, Hurghada, and Marsa Alam) using 10 values in different years with associated rainfall events. This validation was carried out using the following method: (a) drawing a scatter plot between MERRA-2 and the data of the metrological rain gauge stations, which showed a high R2 value (R2 = 0.98) (Figure 7a); (b) for land stations close to the study area, by validating the nearest rain gauge station (Idfu) on 14 January 1997 (rain gauge = 4.7, while MERRA-2 = 4.29) and in May-2020 (rain gauge = 5.4, while MERRA-2 = 5.27), MERRA-2 gave high accuracy; and (c) calibration of Hurghada station in October-2016 (rain gauge = 51.6, while MERRA-2 = 36.9) and Aswan station in May-1993 (rain gauge = 0.5, while MERRA-2 = 0), which showed that MERRA-2 is a conservative (underestimating) value. For the second method, we used daily soil moisture index (SMI) data available from [75], but unfortunately the lack of data before 2007 prevented the confirmation of all storms. Therefore, we are focused on the storm of 26–27 October 2016 by measuring the SMI during and after the effects of the storms (Figure 7b,c).

Figure 7d illustrates the rainfall accumulation comparison between the upstream and downstream regions of the study area during a 39-year period (1981–2019). The topographic effects were strongly reflected in the rainfall distribution. The upstream parts of the basin (1043 m a.s.l.) received significantly more rainfall than the lower parts of the basin, which received <20 mm near the Nile River. Despite the paucity of rainfall in the study area, occasional flash flood events are recorded in the study area once every 3 to 4 years, especially in the Eastern Desert. These flash floods are very important for recharging groundwater aquifers. Many storms occurred in the last four decades. The investigation of the obtained rainfall data showed that the biggest rainfall storms that led to flash floods occurred in 1986, 1993, 1997, and 2016. Climate change has had a significant impact on the reduction in large rainfall storms since 1997.

The rainfall thematic layer (Figure 7e) was constructed using monthly MERRA-2 average annual rainfall data for 39 years (from January 1981 to December 2019) for gridded points and interpolated a raster surface from points using kriging ArcGIS software. The rainfall map was then classified into five zones based on the amount of rainfall. The very low (2.33–3.46 mm), low (3.46–4.15 mm), moderate (4.15–5.08 mm), high (5.08–6.21 mm), and very high (6.21–7.67 mm) rainfall classes covered around 57.7, 21, 11, 5, and 4 percent of the land, respectively. The very high rainfall class and the high-rainfall class were given high weights. The low-rainfall class and very low rainfall class were awarded low weight.
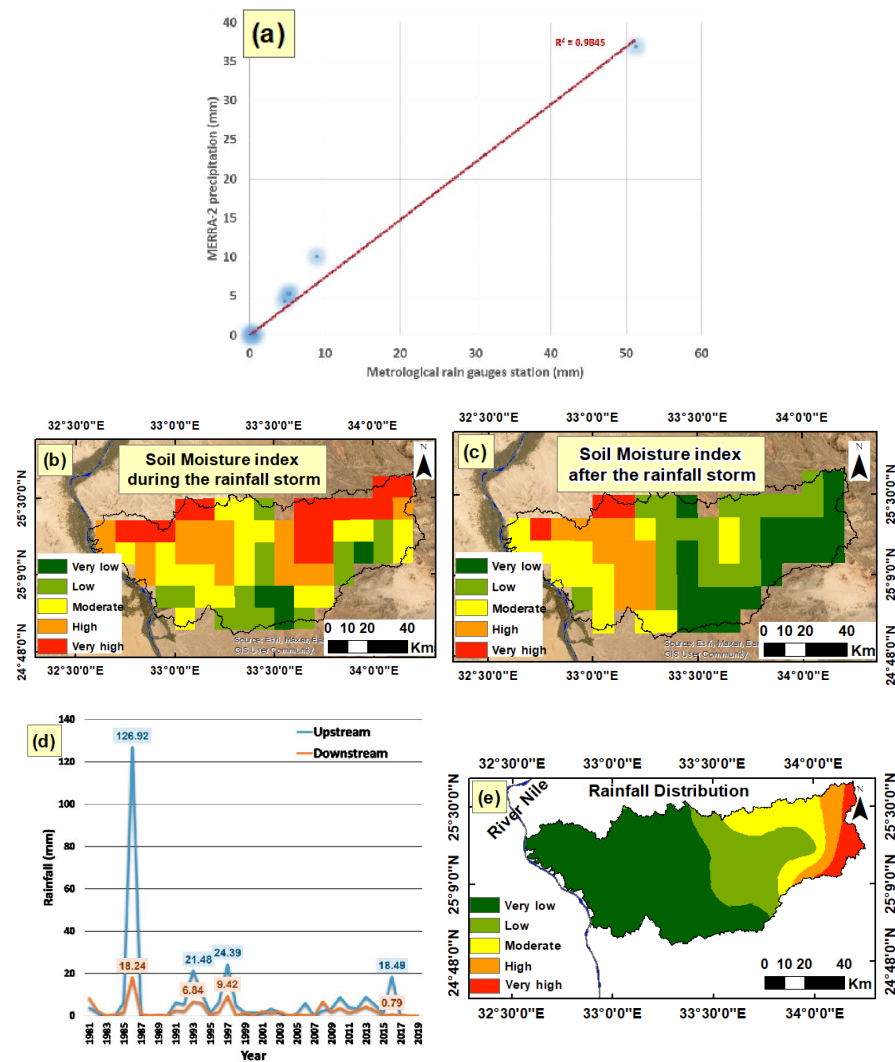
Figure 7. (**a**) Scatter plot of ten values in some rainfall events for validation of MERRA-2 precipitation by meteorological rain gauge stations near the study area (Idfu, Aswan, Luxor, Hurghada, and Marsa Alam) associated with R2; (**b**) Daily soil moisture index (SMI) during the major storm on 26 October 2016; (**c**) Daily soil moisture index (SMI) after the major storm on 28 October 2016; (**d**) A comparison of accumulated annual rainfall between the upstream and downstream parts of the study area during the 39 years from 1981 to 2019; (**e**) Average annual rainfall map of the last four decades (1981–2019).

5.2.5. Structure Lineament Density

Lineament is a significant feature to be considered when investigating groundwater potentiality. Cracks, fissures, faults, shear zones, and joints are formed as a result of the tectonic stress/strain. These linear features, which are considered secondary porosities, are responsible for infiltrating surface runoff and recharging shallow groundwater aquifers. High lineament density correlates strongly to high groundwater potentiality [76–78]. In the eastern part of the study area, basement complex rocks have undergone significant polyphase deformation. Joints, faults, folds, foliations, shear zones, and rock cleavages are all caused by these deformations. Remote sensing data, such as the panchromatic band of Landsat 8 as well the Landsat 8 band combination (7,5,3) were associated with a published geological map [62] to visually extract structure lineaments.

The analysis and investigation of Figure 8a display the spatial distribution of the structure lineaments in the study area. Moreover, the associated rose diagram for these linear features in basement rocks and soft rocks illustrates the major trends of the lineaments. Three significant major trends emerged from the rose diagrams. The NW–SE trend formed

as a result of Red Sea tectonic activity. Furthermore, the NE–SW direction is considered the major structural trend controlling the formation of Wadi Abadi. Moreover, the inspection of a hand-dug well in the Nubian sandstone aquifer (well no. 11) showed the subsurface continuity of that trend in the subsurface succession (Figure 8d). The creation of the porous and permeable zone for probable recharging processes and managing groundwater flow is structurally related, which creates a conduit acting as pipes transferring both groundwater and surface water. Moreover, the NW–SE and NNE–SSW trends that characterize the Arabian-Nubian Shield across the Eastern Desert of Egypt have been detected in the study area (Figure 8e). The lineament density was computed using Equation (4) of [79].

$$\text{Ld} = \frac{\sum_{i=1}^{i=n} L}{A} \ (\text{km}^{-1}) \tag{4}$$
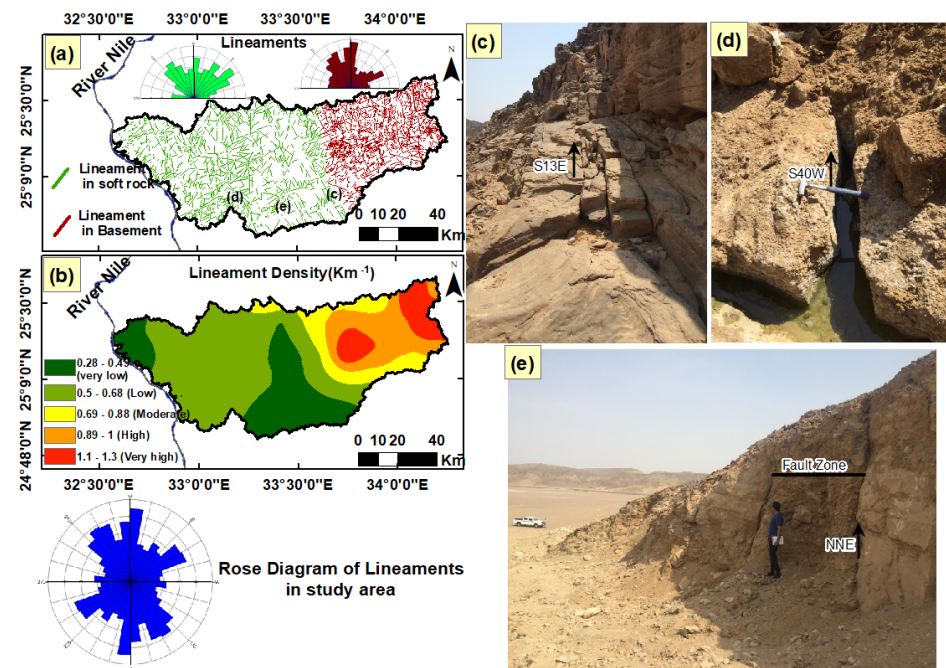
Figure 8. (**a**) Structure lineament network extracted from Landsat image and geologic maps. Rose diagrams for lineaments in basement and sedimentary rocks are also shown to illustrate the major trends controlling the groundwater recharge and flow; (**b**) Thematic layer of structure the lineament density map; (**c**) The NW–SE trend of fracture set in Nubia Sandstone exposures in Wadi Abadi; (**d**) The NE–SW trend of fracture was detected at the Nubia aquifer at the bottom of hand-dug well 11 in Wadi Abadi; (**e**) The trends of dominated fractures are NW–SE and NNE–SSW, which cross Wadi Abadi.

The estimated average lineament density was 0.67 km^{-1} for the whole study area, while the recorded values of the lineament density for the basement and soft rocks were 1 km^{-1} and 0.51 km^{1}, respectively. The higher values of lineament density in basement rocks positively affect the creation of porous and permeable zones favorable for probable recharging processes from precipitation and surface runoff. While the formation of the Nubia Sandstone aquifer was mainly based on its primary porosity between the classic sediments of the aquifer matrix, it was also affected by structural lineaments, raising its potentiality for aquifer recharging. According to these results, the lineament density is one of the most important factors affecting groundwater potentiality in the study area. A lineament density map (Figure 8b) was created by grading the study area by 10 min and splitting it into polygons, then calculating the lineament density for each polygon using the kriging method to interpolate a raster surface from points. The lineament density map was classified into five numerical groups. These classes were very low (0.27–0.49 km^{-1}), low (0.49–0.67 km^{-1}), moderate (0.67–0.87 km^{-1}), high (0.87–1.03 km^{-1}), and very high

(1.03–1.28 km^{-1}). The percentage values of each lineament density class area were around 22, 44, 11, 13.9, and 8 percent of the total surface area of the studied locations, respectively. The very high and high lineament densities were given high weights. The low and very low lineament densities were awarded low weights.

5.2.6. Distance from Major Fractures

In hydrogeological studies, the distance from major fractures is also an important criterion because significant hydrogeological zones must be mainly located close to major linear structures [47]. The extracted map of major faults (Figure 9a) shows the major linear fractures affecting the basement and sedimentary rocks in the study area. The investigation of the rose diagram for these major fractures illustrated that the NNW–SSE trend is the dominant trend in soft rocks. This trend is mainly related to the effect of tectonic activity as a result of Red Sea opening. Moreover, the investigation of Landsat images with the extracted major faults in the arcGIS environment showed that the NNW–SSW trend formed a major graben in the southern part of the study area, especially at Wadi Abadi (Figure 9c,d). This graben was formed along the extension of the red sea trend, where two major faults running through the sandstone plateau were mapped. As a subsided block, the two faults bound the Quseir formation, which is composed of shales and siltstone of the Upper Cretaceous between two main blocks of the Nubian Sandstone (Taref Formation). This structural feature reflects the degree of deformation and tectonic reactivation in the study area, which have positive impacts on enhancing the recharging process for the shallow aquifer from surface runoff and the precipitated rainfall during a major event. Furthermore, the WNW–ESE trend is the dominant trend in the basement rocks in the Arabian-Nubian Shield's extension. In this study, the areas closest to major fractures (400 m) were the most promising for effective infiltration, but as distances increased further than 1000 m, the effect of this parameter vanished (Figure 9b). The area affected by this factor covers about 15% of the study area.
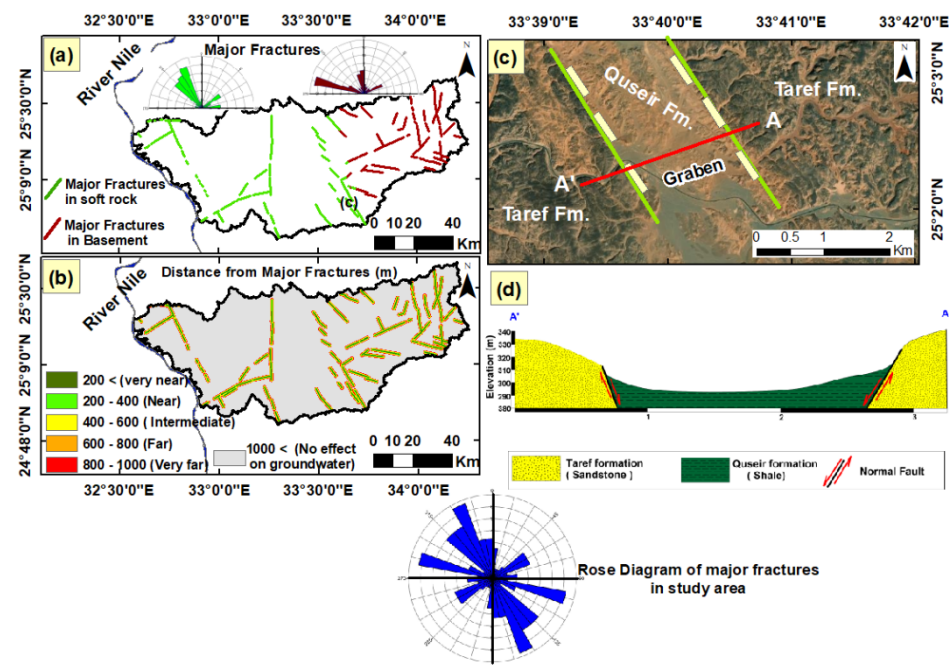
Figure 9. (**a**) Major fractures in basement and sedimentary rocks. Rose diagrams are also shown for major fractures, illustrating the main trends; (**b**) Thematic layer illustrate the distance from major fractures classes and values; (**c**) Close-up view from a satellite image illustrating the faulting processes, which controls both groundwater movement and aquifer recharge; (**d**) Cross section of the exposed rock, illustrating a graben structure formed as a result of two major faults trending NNW–SSE.

5.2.7. Lithology

The thematic layer of lithology is essential in groundwater potential mapping because the porosity and permeability of the surface layer mainly control the infiltration of the precipitated water into the shallow groundwater aquifers [56,57]. The interpretation of the false color composite (FCC) of the Landsat 8 band ratios (3/5, 1/4, and 1/6) associated with a published geological map [62] were used in the lithological discrimination of various rock units (Figure 10a,b). The eastern part of study area is dominated by massive crystalline basement rocks, while the western part is occupied by the Cretaceous/Tertiary succession. The basement rocks, Nubia Sandstone, Upper Cretaceous/Tertiary succession, and Quaternary deposits cover about 29.36, 6.59, 53.9, and 10.15% of the total area, respectively. The porosity and permeability of the Nubia Sandstone Formation and Wadi deposits, which are composed of friable sand and gravel, are great aspects for groundwater recharge. On the other hand, shale and basement rocks have very low permeability characteristics. The Taref Sandstone Formation, which is exposed at the surface in some areas (Figure 10c), dips to the east under the other sedimentary succession to form the Nubia aquifer.
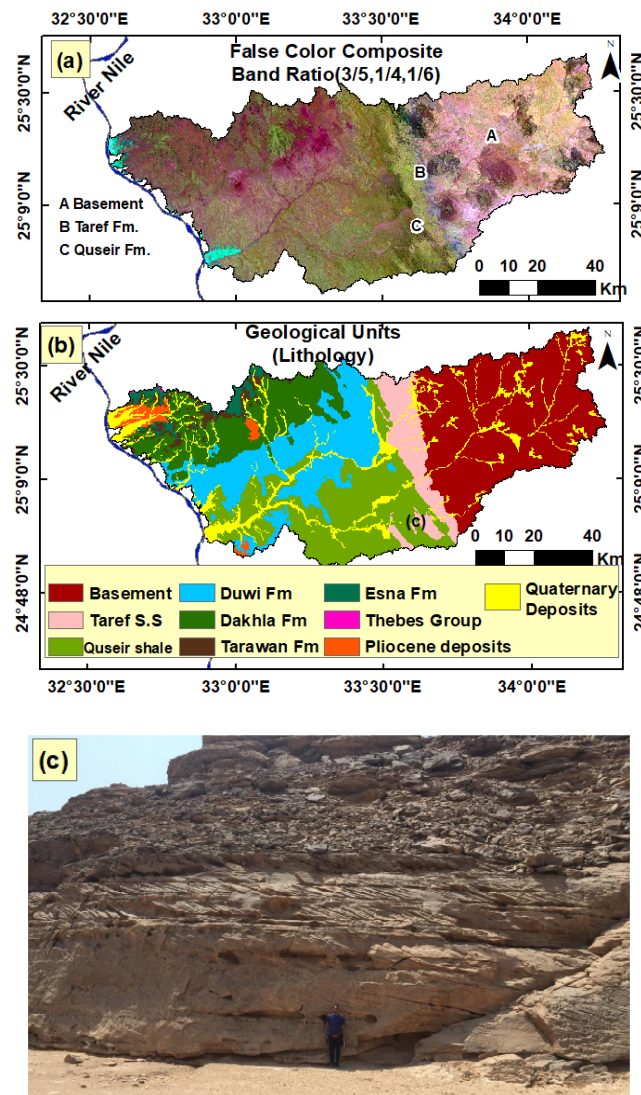
Figure 10. (**a**) False color composite (FCC) of Landsat 8 band ratios (3/5, 1/4, and 1/6); (**b**) Modified geological map (Figure 2) based on band ratios describing the lithology in Table 3; (**c**) Field photo illustrating primary sedimentary structure cross-bedding in Nubia Sandstone in Wadi Abadi.

The porosity and permeability were measured in a core sample from the Nubia Sandstone aquifer at well no. 11 and well no. 18. The measured porosity ranged from 31.02% to 38.36%, while the permeability ranged between 21 millidarcy and 2000 millidarcy. This result illustrates that the Nubia Sandstone aquifer has a different character, with small changes in porosity and extreme changes in permeability from site to site through the study area. The examination of microfacies associations that influence the porosity and permeability in Nubian Sandstone rocks is illustrated in the Supplementary Material.

5.2.8. Land Use/land Cover (LULC)

Groundwater recharging is influenced by the land use/land cover types [52,80–83]. It affects various hydrologic components (surface runoff, infiltration, evapotranspiration, and interception). An LULC map (Figure 11a) was created using a visual interpretation technique that was based on sentinel-2A and verified by Google Earth satellite imagery. Wadi deposits and natural desert grassland are examples of LULC classes that hold significantly higher proportions of water than barren land, rocky surfaces, and mining areas [18,40]. There are five main classes in the study area: barren land, Wadi deposits, mining areas, cultivated land, and natural desert grassland, which cover 88.4, 8.6, 1.3, 1.3, and 0.4 percent of the total area of the studied locations, respectively.
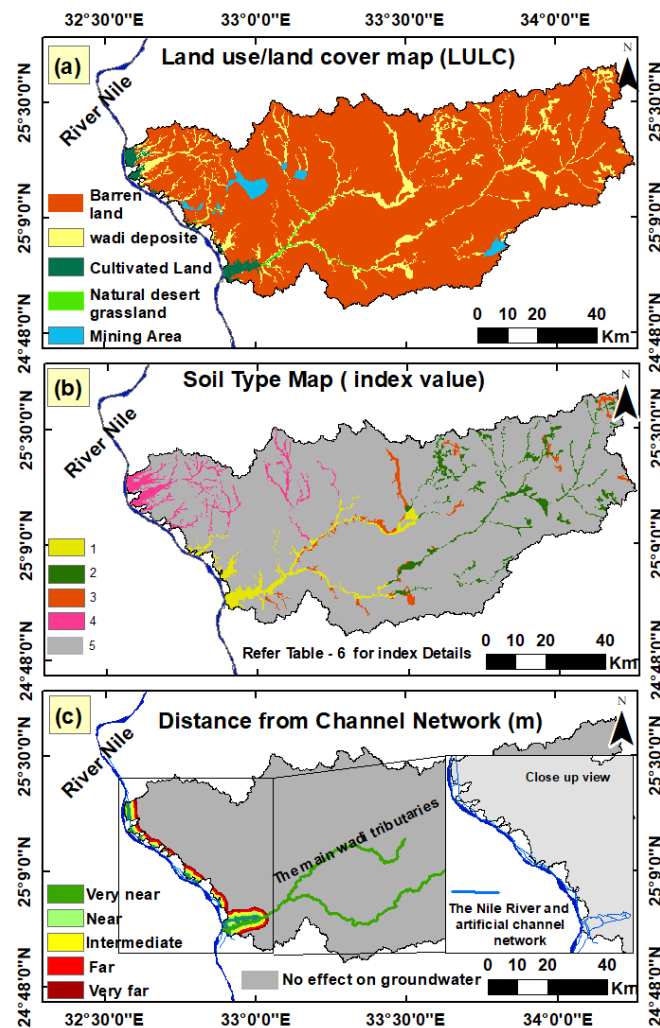
Figure 11. (**a**) The created land use/land cover map (LULC); (**b**) Thematic layer of soil type classes; (**c**) Distance from the channel network, with a close-up view of the Nile river associated with the artificial channel network and the main wadi tributaries crossing the study area.

5.2.9. Soil Type

Soil types determine the amount of water that may percolate into subsurface formations and hence influence groundwater recharge [35,39]. A PCA was created from a Landsat 8 satellite image to distinguish between the different soil types in the Quaternary deposits in the study area. A simplified soil type map was created for the study area based on the field investigation and infiltration test (Figure 11b). The details of the soil types identified in the investigated areas are summarized in Table 6. Sandy gravelly soil infiltrates more rapidly than loamy fine sand soil.

Table 6. The soil types of the study area and their properties, which describe the colors in Figure 11b.

Index	Soil Type
1	• Sandy gravelly soil. • Infiltration capacity equilibrium is about 13.8 mm/min. • Calculated hydraulic conductivity is 7.144×10^{-3} cm/s (very high permeability). • Calculated specific yield (effective porosity) = 31.4%.
2	• Sand to loamy sand soil. • Infiltration capacity equilibrium is about 4.5 mm/min. • Calculated hydraulic conductivity is 4.84×10^{-3} cm/s (high permeability). • Calculated specific yield (effective porosity) = 26%.
3	• Loamy sand soil. • Infiltration capacity equilibrium is about 2 mm/min. • Calculated hydraulic conductivity is 4.84×10^{-3} cm/s (moderately permeability). • Calculated specific yield (effective porosity) = 30%.
4	• Loamy fine sand soil associated with pebbly coarse sand in some parts. • Infiltration capacity equilibrium is about 0.53 mm/min. • Calculated hydraulic conductivity is 1.01×10^{-3} cm/s (low permeability). • Calculated specific yield (effective porosity) = 22%.
5	• Rock land

5.2.10. Distance from Channel Network (DCN)

Groundwater recharge is also influenced by the distance from the surface channel network and water bodies [46,84,85]. In the study area, this factor has a low weight because there is a small contribution of recent Nile water recharge to the Quaternary aquifer but no recent Nile water recharge to the Nubia aquifer [86]. A visual interpretation technique that was based on sentinel-2A and verified by Google Earth satellite imagery was used to extract the channel network. The prepared map (Figure 11c) was divided into five classes, considering acceptable buffer distances from the channel network or water bodies. There was no effect from this factor above 3000 m in distance from a channel network or water body. The main tributaries of Wadi Abadi were considered in this thematic layer, where the main course of the wadi was affected the groundwater recharge, but the locations outside the main channel were less affected.

5.3. The Rainfall Pattern and Return Period in Light of Climatic Change

In light of climatic changes, which have a related impact on water resources, it is necessary to use historical rainfall data in a return period method to identify the rates of rainfall in the future. The repeated maximum precipitation events have a direct relation to the recharging process of the shallow aquifer. A return period analysis for the historical rainfall data during the last four decades was carried out. The calculated results, along with the SWAT model, are useful for estimating the runoff as well as the transmission losses (recharge) for future maximum precipitation events [14,87]. Equation (5) was used to calculate the recurrence interval for precipitation events:

$$R_P = \frac{N + 1}{M} \tag{5}$$

where R_p is the return period, M is the rank of the data corresponding to the event, and N is the number of years of data.

The HEC-DSSVue and HEC-SSP 2.2 programs were used to identify the return period using various statistical distributions. Kolmogorov–Smirnov and chi-square tests were used to evaluate the degree of fitness of probability distribution models with the observed data. Acceptable distributions were graded using two statistics: the mean relative deviation (MRD) and the mean square relative deviation (MSRD), as described in Equations (6) and (7). On the observed data, the distribution with the smallest MRD and MSRD fits the best.

$$\text{M.R.D} = \frac{\sum_{i=1}^{n}|x - \hat{x}|}{(N - m)} \tag{6}$$

$$\text{M.S.R.D} = \frac{\sum_{i=1}^{n}(x - \hat{x})^2}{(N - m)} \tag{7}$$

where x represents the observed data, $\hat{x}$ represents the estimated value, N represents the number of data points, and (m) denotes the number of parameters of the distribution [88]. From an analysis of the average annual accumulation of the study area, an exponential function (Figure 12a) fit the rainfall dataset (1981–2019) best, depending on the MRD and MSRD. The exceedance probability versus the rainfall is illustrated in Figure 12b. The calculated return period rainfall values in Wadi Abadi each 2, 5, 10, 20, and 50 years were 2.95, 6.89, 10.07, 13.25, and 17.39 mm, respectively (Table 7). The lithologic nature of Wadi Abadi is composed of nearly 40% massive rocks (carbonate and basement), which promotes surface runoff from the smallest amount of precipitation. Consequently, the aforementioned amounts of precipitation will participate in creating surface runoff and recharging the shallow aquifer through the transmission losses.


(a)

(b)
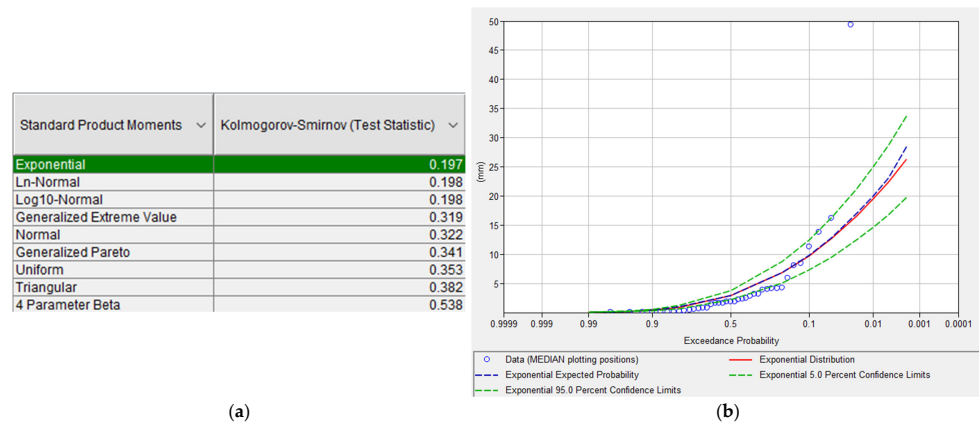
Figure 12. (**a**) Different types of statistical distributions of rainfall data using HEC-SSP2.2 software illustrate that an exponential function had the lowest error in fitting the rainfall dataset for the study area; (**b**) The exceedance probability versus the rainfall using HEC-SSP2.2 software.

Table 7. The HEC-SSP2.2 software was used to calculate the 100-year return period.

Return Period (Years)	Percent Chance Exceedance	Median (mm)	Expected Probability (mm)	Confidence Limits Probability 5% (mm)	Confidence Limits Probability 95% (mm)
2	50	2.934	2.952	3.759	2.196
5	20	6.812	6.894	8.728	5.099
10	10	9.746	10.074	12.487	7.295
20	5	12.679	13.245	16.246	9.492
50	2	16.557	17.393	21.215	12.395
100	1	19.491	20.477	24.974	14.591

The Impact of Climate Change on Groundwater Recharge

Globally, water resources such as groundwater will be impacted directly and indirectly by climate change [89,90]. The results can be used to evaluate the effects of global warming and climate change at a local scale. They offer the effects of the climate change information with a higher resolution. By analyzing the biggest precipitation events in the last four decades in the Abadi basin, the largest precipitation was about 48 mm in 1986, and this has not been repeated (Figure 13). Since 1997, this area has lacked high precipitation for about 20 years (Figure 7d). The recent major precipitation in 2016 was only 7.25 mm. It is expected that a detected major storm (maximum precipitation in one day) could enhance the groundwater recharge to the shallow aquifer in the Abadi basin. On the other hand, the decrease in the precipitation amount could cause the aquifer to deteriorate over time due and reduce the groundwater recharge. The amount of precipitation based on the return period for the next 50 years is only 17.4 mm. The predicted low recharges due to the effects of climate change need more groundwater management for sustainable development. The other wadies, especially in the Esna area, suffer from the reduction in the amount of precipitation for the last four decades.
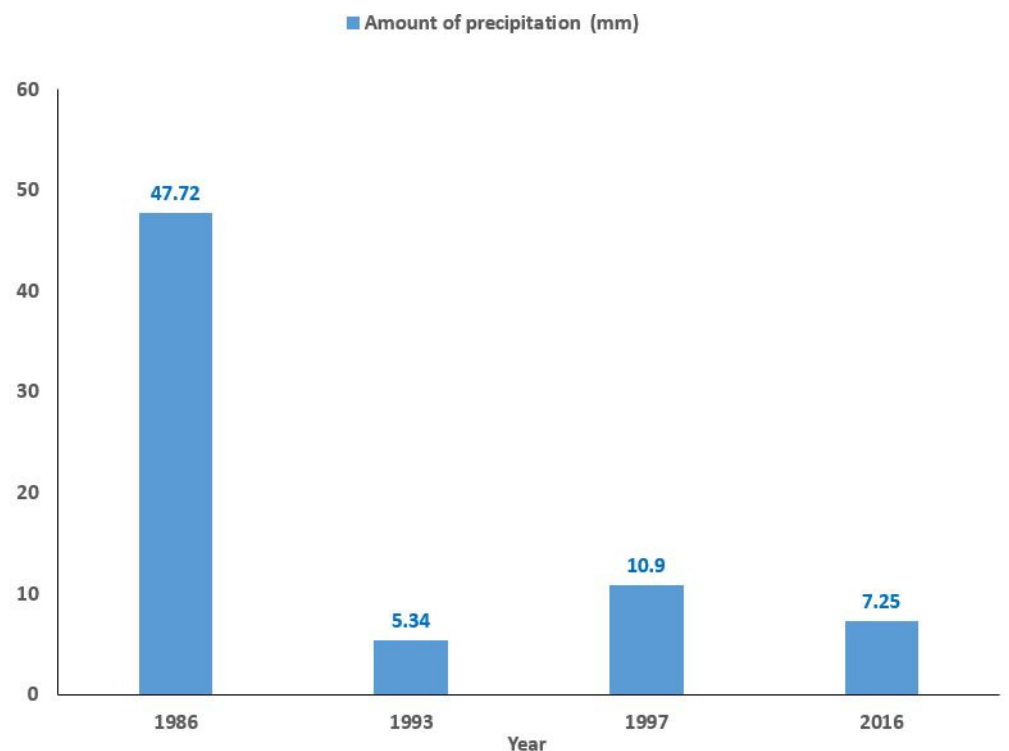
Figure 13. The precipitation and related recharge to the main aquifer in the Abadi basin in major rainfall events in the last four decades.

5.4. Groundwater Potential Zone (GWPZ)

The groundwater potential zone (GWPZ) map was created using a weighted overlay model that divided the study area into three classes: poor, moderate, and good potential recharge zones occupying 7073.47 km^2 (88.6%), 625.08 km^2 (7.8%), and 281.23 km^2 (3.52%) of the total surface area of the studied locations (Figure 14). The downstream portion of the studied wadies in the northwestern part of the study area near Esna has moderate potentiality (Figure 14a). Good potential zones are concentrated in the southwestern part (Figure 14b) and basement area (Figure 14c). The lineament density and major fractures play a major role in the groundwater potential recharge in the basement area. The result of the petrographic analysis illustrates that the Nubia Sandstone aquifer changes its character throughout the study area and that major fractures play a significant role in groundwater

movement and recharging processes. Based on a pumping test downstream of Wadi Abadi, the values of transmissivity were calculated, and they ranged between 78 m^2/day (well 19) and 346.3 m^2/day (well 13). The return period and rainfall analyses were used to predict the precipitation in the future for 100 years, illustrating that precipitation is limited and groundwater potentiality should be managed. On the other hand, the analysis and examination of the rainfall data over the study area for the last four decades using satellite-based spatial and temporal precipitation (MERRA-2) data were carried out. Our analysis showed that the largest precipitation events occurred in the Wadi Abadi basin, which experienced average annual precipitation through the last four decades of 7.67 mm, while the northwestern part of the study area in the El-Dir basin received only 91 mm. Moreover, the applied weighted overlay model of potential recharging zones illustrated that the good potential recharge areas are located in Wadi Abadi, especially in the upstream portion and some sites in the downstream area (Figure 14b,c). However, the result of the weighted overlay model of Wadi El-Dir showed that it falls within the moderate zone of potential recharge for groundwater, but no recharging from groundwater reaching the aquifer was observed, and a remarkable drop in the water level for the Quaternary aquifer was detected from 2014, ranging from 2 m proximal to the Nile River to 14 m distal from the river Nile (Figure 15). This drawdown could be related to two reasons: (a) low rainfall, which leads to a low recharge rate, and (b) overpumping, where the locals use flood irrigation to farm their lands. Therefore, more hydrological studies are required in order to determine the hydraulic properties of the Quaternary aquifer and to identify the safe discharge from the wells to protect the aquifer from deterioration.
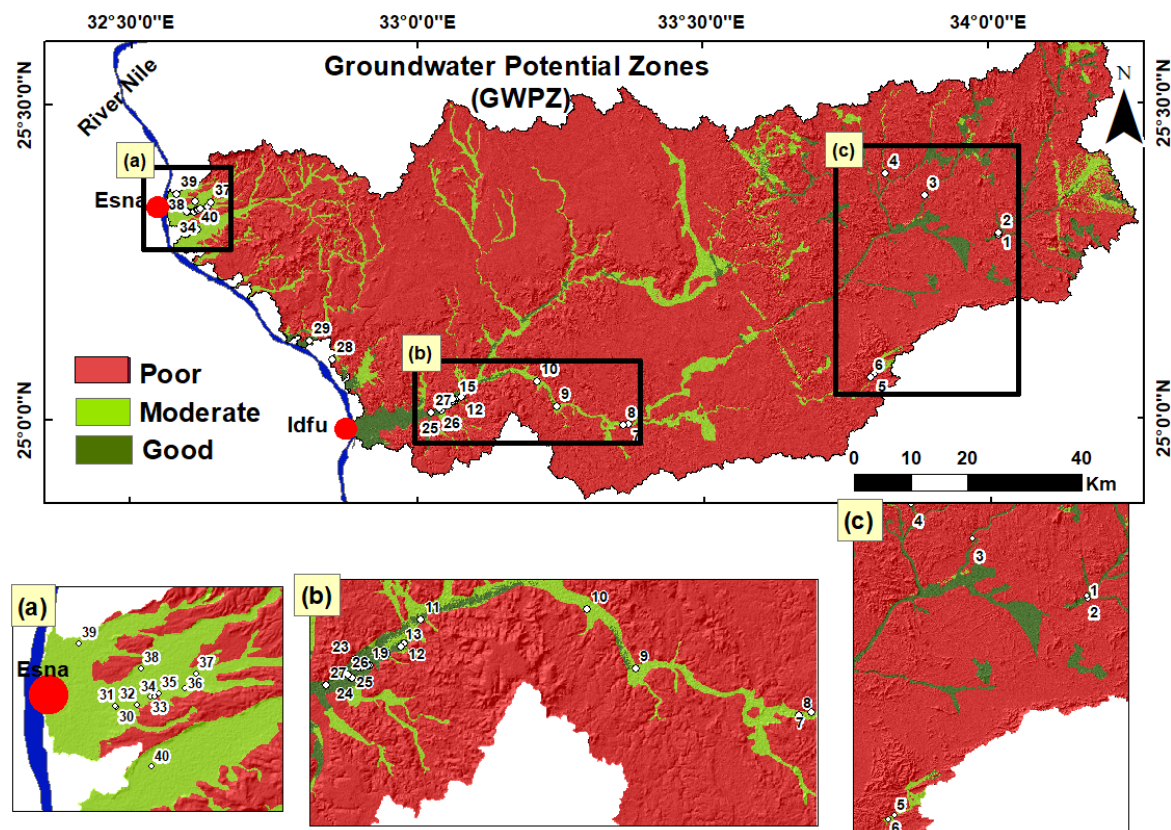
Figure 14. Groundwater potential zone map (GWPZ) associated with observation wells draped over a hill-shaded relief map illustrating the classes of potential recharge zoning; (**a**) observation wells in the Esna area; (**b**) observation wells in the Idfu area; (**c**) observation wells in the basement area at Wadi Abadi.
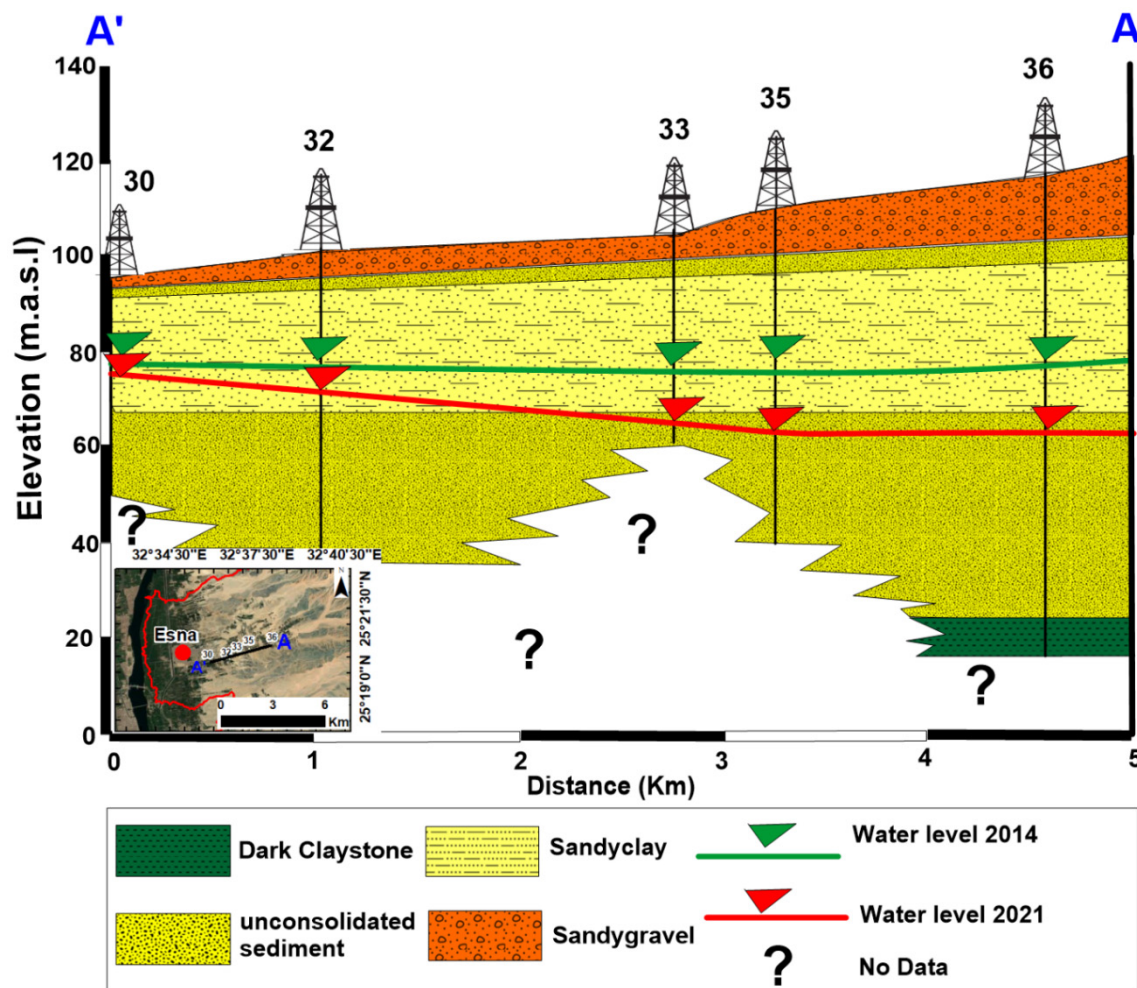
Figure 15. Subsurface hydrogeological cross section (A'-A) showing the drop in the static water level during the period from 2014 to 2021 at 5 wells in the Quaternary aquifer at Wadi El-Dir.

5.5. Model Validation

The water level data (depth to water) were detected at 40 observed wells (Figure 14a–c) of the study area. The validation was based on (a) the depth to water and (b) the drawdown in the water level through 7 years (2015–2021), which illustrates that the Wadi El-Dir area suffers from a drop in the water level (2–14 m), so it shows moderate potential recharge. On the other hand, the recorded drawdown in Wadi Abadi ranged from 0.5 m to 1.5 m within the same period, taking into consideration that they had nearly the same discharge for irrigation activity. (c) The high values of transmissivity in some wells downstream of Wadi Abadi ranged from 78 m^2/day (well 19) to 346.3 m^2/day (well 13), reflecting the high potentiality of the aquifer in this area. The poor zone mainly falls within the highly mountainous and/or hilly areas that are not prospected locations for groundwater exploration or development. The values used to validate the groundwater potential zone map reflect the actual recharge condition and the groundwater potential in certain locations. A comparison study was performed between the groundwater level in each well and the groundwater potential zones. (Table 8). The validation conclusions show that about 82.5 percent of the wells correctly fit the zonation of the groundwater potential map.

$$\text{Overall accuracy} = \frac{\text{Number of correct Observation well location}}{\text{Total number of Observation well location}} = \frac{33}{40} = 82 \tag{8}$$

Table 8. Groundwater level accuracy assessment of the GWPZ map.

S No.	Aquifer type	Basin	Well Type	Latitude	Longitude	Depth to Water (2015–2021)			Groundwater Level	Well Location on GWPZ Map	Validation Remarks
						2015	2021	Drawdown			
1				25.29305	34.01715	21	-	-	Medium	Poor	Disagree
2				25.2962	34.01673	13.5	-	-	Shallow		
3	Basement	Abadi	Hand-dug	25.35523	33.8881	11.22	-	-	Shallow	Good	Agree
4				25.39138	33.8192	3.31	-	-	Very Shallow		
5				25.07295	33.79751	-	36.3	-	Medium	Moderate	
6				25.06789	33.79088	-	32.8	-			
7			Drilled	24.99508	33.36889	-	60	-	Medium/Deep	Moderate	Partially agree
8				24.99331	33.35946	-	55	-			
9	Nubia	Abadi		25.02363	33.24399	-	44	-	Medium		Agree
10				25.06227	33.20951	-	32.3	-	Medium		Agree
11			Hand-dug	25.05524	33.09096	8.5	10	1.5	Shallow	Good	Agree
12				25.03958	33.07906	-	10.2	-	Shallow	Good	Agree
13				25.03756	33.07654	8.7	10	1.3	Shallow	Good	Agree
14				25.03233	33.06653	7.5	8	0.5	Very Shallow	Good	Agree
15			Drilled	25.03411	33.06639	10	11	1	Shallow	Moderate	Partially agree
16				25.03237	33.06243	-	15.8	-	Shallow		
17				25.03537	33.062	-	4.2	-	Very Shallow		
18				25.02555	33.05486	8.6	10	1.4	Shallow	Good	Agree
19				25.02591	33.05341	-	12	-	Shallow		
20				25.02426	33.04908	5	6	1	Very Shallow		
21	Quaternary		Hand-dug	25.02464	33.04648	4	5.2	1.2	Very Shallow	Good	Agree
22	Nubia			25.02999	33.04420	-	6.7	-	Very Shallow	Good	Agree
23		Abadi	Drilled	25.0296	33.04430	-	7.8	-			Agree
24				25.0177	33.04155	3	4	1			Agree
25	Quaternary		Hand-dug	25.01735	33.04177	2.9	4.2	1.3			Agree
26				25.01964	33.03901	-	4.1	-	Very Shallow	Good	Agree
27				25.0128	33.02373	-	3	-			Agree
28		Al-Mafallis	Drilled	25.09834	32.85235	-	2.9	-		Moderate	Disagree
29	Nubia	Hilal	Spring	25.12756	32.81267	Flowing			Very Shallow	Good	Agree
30				25.33117	32.59856	18	20	2			
31				25.33142	32.59790	18	20	2			
32				25.33219	32.60896	25	30	5	Medium		Agree
33		El-Dir		25.33567	32.61537	30	40	10			
34	Quaternary		Drilled	25.33562	32.61775	-	44.6	-		Moderate	
35				25.33738	32.61988	35	47	12			
36				25.33968	32.63270	40	54	14	Medium/Deep		Partially agree
37				25.34631	32.6385	-	63	-	Medium/Deep		
38				25.34867	32.611	-	32	-			
39		El-Foley		25.35972	32.57956	-	20	-	Medium		Agree
40		El-Sabil		25.30405	32.61621	-	36	-			

6. Conclusions

An integrated approach using remote sensing datasets, including Landsat, sentinel images, and a digital elevation model, along with field investigation and GIS modeling was conducted to delineate groundwater potential zones in arid environments. The spatial analysis gained from the remote sensing datasets with geologic maps and field investigations revealed that the study area is highly affected by the structure discontinuity appearing in the extensive lineament network and major fractures. This fracture system, which is considered a main factor in the applied GIS model, has a directly impact on groundwater recharge and identifying potential zones. The major findings are (1) remote sensing and GIS in conjunction with the AHP method are effective techniques for delineating a groundwater potential map with accuracy (82.5%); (2) the analysis of historical rainfall data for last 39 years revealed that the study area had not received any significant precipitation since 1997, which was nearly 20 years, due to the effects of climatic changes; (3) by comparing the static water levels in 2014 and 2021 at five wells in Wadi El-Dir, there were drawdowns in the water levels ranging from 2 to 14 m due to the excessive discharge and the lack of rainfall in this area; and (4) the estimated porosity of the Nubia Sandstone aquifer in the

middle and downstream parts of Wadi Abadi revealed that the porosity ranged from 31 to 38% and the permeability ranged from 21 to 2000 millidarcy.

The integration of remote sensing datasets with field investigations and GIS technologies is very effective for improving the results of preliminarily examinations for groundwater exploration in areas where well data are scarce. The application of this approach is cost-effective in arid environments and developing countries and could be applicable for similar regions worldwide.

References

1. Yousif, M. A new theory to enhance the groundwater-related decisions based on deciphering the palaeohydrologic regime under climate change in the Sahara. *Model. Earth Syst. Environ.* **2021**, *8*, 3885–3895. [CrossRef]
2. Yousif, M.; Hussien, H.M.; Abotalib, A.Z. The Respective roles of modern and paleo recharge to alluvium aquifers in continental rift basins: A case study from El Qaa Plain, Sinai, Egypt. *Sci. Total Environ.* **2020**, *739*, 139927. [CrossRef] [PubMed]
3. UNESCO. *The United Nations World Water Development Report 2015*; Water for a Sustainable World; UNESCO: Paris, France, 2015.
4. Ghosh, D.; Mandal, M.; Karmakar, M.; Banerjee, M.; Mandal, D. Application of geospatial technology for delineating groundwater potential zones in the Gandheswari Watershed, West Bengal. *Sustain. Water Resour. Manag.* **2020**, *6*, 1–14. [CrossRef]
5. Global Information System on Water and Agriculture. Available online: https://www.fao.org/aquastat/en/databases/ (accessed on 4 December 2021).
6. Heggy, E.; Sharkawy, Z.; Abotalib, A.Z. Egypt's water budget deficit and suggested mitigation policies for the grand ethiopian renaissance dam filling scenarios. *Environ. Res. Lett.* **2021**, *16*, 074022. [CrossRef]
7. Senanayake, I.P.; Dissanayake, D.M.D.O.K.; Mayadunna, B.B.; Weerasekera, W.L. An approach to delineate groundwater recharge potential sites in Ambalantota, Sri Lanka using GIS techniques. *Geosci. Front.* **2016**, *7*, 115–124. [CrossRef]
8. Jha, M.K.; Chowdary, V.M.; Chowdhury, A. Groundwater assessment in Salboni Block, West Bengal (India) using remote sensing, geographical information system and multi-criteria decision analysis techniques. *Hydrogeol. J.* **2010**, *18*, 1713–1728. [CrossRef]
9. Jha, M.K.; Chowdhury, A.; Chowdary, V.M.; Peiffer, S. Groundwater management and development by integrated remote sensing and geographic information systems: Prospects and constraints. *Water Resour. Manag.* **2007**, *21*, 427–467. [CrossRef]
10. Israil, M.; Al-hadithi, M.; Singhal, D.C. Application of a resistivity survey and geographical information system (GIS) analysis for hydrogeological zoning of a Piedmont Area, Himalayan Foothill Region, India. *Hydrogeol. J.* **2006**, *14*, 753–759. [CrossRef]
11. Oh, H.J.; Kim, Y.S.; Choi, J.K.; Park, E.; Lee, S. GIS mapping of regional probabilistic groundwater potential in the area of Pohang City, Korea. *J. Hydrol.* **2011**, *399*, 158–172. [CrossRef]
12. Adiat, K.A.N.; Nawawi, M.N.M.; Abdullah, K. Assessing the accuracy of GIS-based elementary multi criteria decision analysis as a spatial prediction tool—A case of predicting potential zones of sustainable groundwater resources. *J. Hydrol.* **2012**, *440–441*, 75–89. [CrossRef]

13. Russo, T.A.; Fisher, A.T.; Lockwood, B.S. Assessment of managed aquifer recharge site suitability using a GIS and modeling. *Groundwater* **2015**, *53*, 389–400. [CrossRef] [PubMed]

14. Hussien, H.M.; Kehew, A.E.; Aggour, T.; Korany, E.; Abotalib, A.Z.; Hassanein, A.; Morsy, S. An integrated approach for identification of potential aquifer zones in structurally controlled terrain: Wadi Qena Basin, Egypt. *Catena* **2017**, *149*, 73–85. [CrossRef]

15. Tiwari, K.; Goyal, R.; Sarkar, A. GIS-based spatial distribution of groundwater quality and regional suitability evaluation for drinking water. *Environ. Process.* **2017**, *4*, 645–662. [CrossRef]

16. Arulbalaji, P.; Padmalal, D.; Sreelash, K. GIS and AHP techniques based delineation of groundwater potential zones: A case study from Southern Western Ghats, India. *Sci. Rep.* **2019**, *9*, 1–17. [CrossRef]

17. Hussien, H.M.; Yousif, M.; El Sheikh, A. Investigation of groundwater occurrences in structurally controlled terrain, based on geological studies and remote sensing data: Wadi El Morra, South Sinai, Egypt. *NRIAG J. Astron. Geophys.* **2020**, *9*, 512–531. [CrossRef]

18. Madani, A.; Niyazi, B. Groundwater potential mapping using remote sensing techniques and weights of evidence GIS model: A case study from Wadi Yalamlam Basin, Makkah Province, Western Saudi Arabia. *Environ. Earth Sci.* **2015**, *74*, 5129–5142. [CrossRef]

19. Fildes, S.G.; Clark, I.F.; Somaratne, N.M.; Ashman, G. Mapping Groundwater potential zones using remote sensing and geographical information systems in a fractured rock setting, southern flinders ranges, South Australia. *J. Earth Syst. Sci.* **2020**, *129*, 1–25. [CrossRef]

20. Srinivasa Rao, Y.; Jugran, D.K. Delineation of Groundwater potential zones and zones of groundwater quality suitable for domestic purposes using remote sensing and GIS. *Hydrol. Sci. J.* **2003**, *48*, 821–833. [CrossRef]

21. Kumar, P.K.D.; Gopinath, G.; Seralathan, P. International journal of remote application of remote sensing and GIS for the demarcation of groundwater potential zones of a River Basin in Kerala, Southwest Coast of India. *Int. J. Remote Sens.* **2007**, *28*, 5583–5601. [CrossRef]

22. Prasad, R.K.; Monda, N.C.; Banerjee, P.; Nandakumar, M.V.; Singh, V.S. Deciphering Potential Groundwater Zone in Hard Rock Through The Application of GIS. *Environ. Geol.* **2008**, *55*, 467–475. [CrossRef]

23. Ganapuram, S.; Kumar, G.T.V.; Krishna, I.V.M.; Kahya, E.; Demirel, M.C. Mapping of groundwater potential zones in the Musi Basin using remote sensing data and GIS. *Adv. Eng. Softw.* **2009**, *40*, 506–518. [CrossRef]

24. Al Saud, M. Mapping potential areas for groundwater storage in Wadi Aurnah Basin, Western Arabian Peninsula, using remote sensing and geographic information system techniques. *Hydrogeol. J.* **2010**, *18*, 1481–1495. [CrossRef]

25. Avtar, R.; Singh, C.K.; Shashtri, S.; Singh, A.; Mukherjee, S. Identification and analysis of groundwater potential zones in Ken-Betwa River linking area using remote sensing and geographic information system. *Geocarto Int.* **2010**, *25*, 379–396. [CrossRef]

26. Dar, I.A.; Sankar, K.; Dar, M.A. Remote sensing technology and geographic information system modeling: An integrated approach towards the mapping of groundwater potential zones in Hardrock Terrain, Mamundiyar Basin. *J. Hydrol.* **2010**, *394*, 285–295. [CrossRef]

27. Elewa, H.H.; Qaddah, A.A. Groundwater potentiality mapping in the Sinai Peninsula, Egypt, using remote sensing and GIS-watershed-based modeling. *Hydrogeol. J.* **2011**, *19*, 613–628. [CrossRef]

28. Abdelkareem, M.; El-Baz, F.; Askalany, M.; Akawy, A.; Ghoneim, E. Groundwater prospect map of Egypt's Qena Valley Using data fusion. *Int. J. Image Data Fusion* **2012**, *3*, 169–189. [CrossRef]

29. Magesh, N.S.; Chandrasekar, N.; Soundranayagam, J.P. Delineation of groundwater potential zones in Theni District, Tamil Nadu, using remote sensing, GIS and MIF techniques. *Geosci. Front.* **2012**, *3*, 189–196. [CrossRef]

30. Abdalla, F. Mapping of groundwater prospective zones using remote sensing and GIS techniques: A case study from the Central Eastern Desert, Egypt. *J. African Earth Sci.* **2012**, *70*, 8–17. [CrossRef]

31. Deepika, B.; Avinash, K.; Jayappa, K.S. Integration of hydrological factors and demarcation of groundwater prospect zones: Insights from remote sensing and GIS techniques. *Environ. Earth Sci.* **2013**, *70*, 1319–1338. [CrossRef]

32. Nag, S.K.; Ghosh, P. Delineation of groundwater potential zone in Chhatna Block, Bankura District, West Bengal, India using remote sensing and GIS techniques. *Environ. Earth Sci.* **2013**, *70*, 2115–2127. [CrossRef]

33. Nampak, H.; Pradhan, B.; Manap, M.A. Application of GIS based data driven evidential belief function model to predict groundwater potential zonation. *J. Hydrol.* **2014**, *513*, 283–300. [CrossRef]

34. Agarwal, R.; Garg, P.K. Remote sensing and GIS based groundwater potential & recharge zones mapping using multi-criteria decision making technique. *Water Resour. Manag.* **2016**, *30*, 243–260. [CrossRef]

35. Ibrahim-Bathis, K.; Ahmed, S.A. Geospatial technology for delineating groundwater potential zones in Doddahalla Watershed of Chitradurga District, India. *Egypt. J. Remote Sens. Sp. Sci.* **2016**, *19*, 223–234. [CrossRef]

36. Selvarani, A.G.; Maheswaran, G.; Elangovan, K. Identification of artificial recharge sites for Noyyal River Basin using GIS and remote sensing. *J. Indian Soc. Remote Sens.* **2017**, *45*, 67–77. [CrossRef]

37. Hussein, A.-A.; Govindu, V.; Nigusse, A.G.M. Evaluation of groundwater potential using geospatial techniques. *Appl. Water Sci.* **2017**, *7*, 2447–2461. [CrossRef]

38. Thapa, R.; Gupta, S.; Guin, S.; Kaur, H. Assessment of groundwater potential zones using multi-influencing factor (MIF) and GIS: A case study from Birbhum District, West Bengal. *Appl. Water Sci.* **2017**, *7*, 4117–4131. [CrossRef]

39. Das, S. Delineation of groundwater potential zone in hard rock terrain in Gangajalghati Block, Bankura District, India using remote sensing and GIS techniques. *Model. Earth Syst. Environ.* **2017**, *3*, 1589–1599. [CrossRef]
40. Rajaveni, S.P.; Brindha, K.; Elango, L. Geological and geomorphological controls on groundwater occurrence in a hard rock region. *Appl. Water Sci.* **2017**, *7*, 1377–1389. [CrossRef]
41. Patra, S.; Mishra, P.; Mahapatra, S.C. Delineation of groundwater potential zone for sustainable development: A case study from Ganga Alluvial plain covering Hooghly District of India using remote sensing, geographic information system and analytic hierarchy process. *J. Clean. Prod.* **2018**, *172*, 2485–2502. [CrossRef]
42. Adeyeye, O.A.; Ikpokonte, A.E.; Arabi, A.S. The dual use of drainage characteristics in groundwater potential modelling using remote sensing and GIS: An example from Dengi Area, Northcentral Nigeria. *Sustain. Water Resour. Manag.* **2018**, *4*, 1105–1115. [CrossRef]
43. Pande, C.B.; Khadri, S.F.R.; Moharir, K.N.; Patode, R.S. Assessment of groundwater potential zonation of Mahesh River Basin Akola and Buldhana Districts, Maharashtra, India using remote sensing and GIS techniques. *Sustain. Water Resour. Manag.* **2018**, *4*, 965–979. [CrossRef]
44. Murmu, P.; Kumar, M.; Lal, D.; Sonker, I.; Singh, S.K. Delineation of groundwater potential zones using geospatial techniques and analytical hierarchy process in Dumka District, Jharkhand, India. *Groundw. Sustain. Dev.* **2019**, *9*, 100239. [CrossRef]
45. Çelik, R. Evaluation of groundwater potential by GIS-Based multicriteria decision making as a spatial prediction tool: Case study in the Tigris River Batman-Hasankeyf Sub-Basin, Turkey. *Water* **2019**, *11*, 2630. [CrossRef]
46. Mallick, J.; Khan, R.A.; Ahmed, M.; Alqadhi, S.D.; Alsubih, M.; Falqi, I.; Hasan, M.A. Modeling groundwater potential zone in a Semi-Arid Region of Aseer using Fuzzy-AHP and geoinformation techniques. *Water* **2019**, *11*, 2656. [CrossRef]
47. Benjmel, K.; Amraoui, F.; Boutaleb, S.; Ouchchen, M.; Tahiri, A.; Touab, A. Mapping of groundwater potential zones in techniques, and multicriteria data analysis (Case of the Ighrem Region, Western Anti-Atlas, Morocco). *Water* **2020**, *12*, 471. [CrossRef]
48. Achu, A.L.; Reghunath, R.; Thomas, J. Mapping of groundwater recharge potential zones and identification of suitable site-specific recharge mechanisms in a tropical river basin. *Earth Syst. Environ.* **2020**, *4*, 131–145. [CrossRef]
49. Berhanu, K.G.; Hatiye, S.D. Identification of groundwater potential zones using proxy data: Case study of Megech Watershed, Ethiopia. *J. Hydrol. Reg. Stud.* **2020**, *28*, 100676. [CrossRef]
50. Lentswe, G.B.; Molwalefhe, L. Delineation of potential groundwater recharge zones using analytic hierarchy process-guided GIS in the semi-arid Motloutse Watershed, Eastern Botswana. *J. Hydrol. Reg. Stud.* **2020**, *28*, 100674. [CrossRef]
51. Mukherjee, I.; Singh, U.K. Delineation of groundwater potential zones in a drought-prone semi-arid region of East India using GIS and analytical hierarchical process techniques. *Catena* **2020**, *194*, 104681. [CrossRef]
52. Kaur, L.; Rishi, M.S.; Singh, G.; Nath Thakur, S. Groundwater potential assessment of an alluvial aquifer in Yamuna Sub-Basin (Panipat Region) using remote sensing and GIS techniques in conjunction with Analytical Hierarchy Process (AHP) and Catastrophe Theory (CT). *Ecol. Indic.* **2020**, *110*, 105850. [CrossRef]
53. Ahmadi, H.; Kaya, O.A.; Babadagi, E.; Savas, T.; Pekkan, E. GIS-based groundwater potentiality mapping using AHP and FR models in Central Antalya, Turkey. *Environ. Sci. Proc.* **2021**, *5*, 11. [CrossRef]
54. Zhu, Q.; Abdelkareem, M. Mapping groundwater potential zones using a knowledge-driven approach and GIS analysis. *Water* **2021**, *13*, 579. [CrossRef]
55. Ranganathan, M.; Murugesan, B.; Mukesh, M.; Islam, Z.; Gebremedhin, D.T.; Brhane, G.K. Groundwater potentiality mapping in Viruthachalam Taluk, Tamil Nadu, India: AHP and GIS approaches. *Hydrospatial Anal.* **2021**, *5*, 24–33. [CrossRef]
56. Anteneh, Z.L.; Alemu, M.M.; Bawoke, G.T.; Kehali, A.T.; Fenta, M.C.; Desta, M.T. Appraising groundwater potential zones using geospatial and Multi-Criteria Decision Analysis (MCDA) techniques in Andasa-Tul Watershed, Upper Blue Nile Basin, Ethiopia. *Environ. Earth Sci.* **2022**, *81*, 1–20. [CrossRef]
57. Melese, T.; Belay, T. Groundwater potential zone mapping using analytical hierarchy process and GIS in Muga Watershed, Abay Basin, Ethiopia. *Glob. Chall.* **2022**, *6*, 2100068. [CrossRef]
58. Ramachandra, M.; Babu, K.R.; Kumar, B.P.; Rajasekhar, M. Deciphering groundwater potential zones using AHP and geospatial modelling approaches: A case study from YSR District, Andhra Pradesh, India. *Int. J. Energy Water Resour.* **2022**, 1–11. [CrossRef]
59. Ogungbade, O.; Ariyo, S.O.; Alimi, S.A.; Alepa, V.C.; Aromoye, S.A.; Akinlabi, O.J. A combined GIS, remote sensing and geophysical methods for groundwater potential assessment of Ilora, Oyo Central, Nigeria. *Environ. Earth Sci.* **2022**, *81*, 1–13. [CrossRef]
60. NASA Prediction of Worldwide Energy Resources Data Access Documentation Resources about Contact. Available online: https://power.larc.nasa.gov/data-access-viewer/ (accessed on 14 October 2021).
61. Izz, A.A. *Landforms of Egypt*; American University Press: Cairo, Egypt, 1971.
62. Conco, C. *Geological Map of Egypt, Scale 1: 500,000*; Egyptian General Petroleum Corporation: Cairo, Egypt, 1987.
63. USGS Earth Explorer. Available online: https://earthexplorer.usgs.gov/ (accessed on 14 October 2021).
64. Saaty, T.L. *Decision Making for Leaders: The Analytic Hierarchy Process for Decisions in a Complex World*; RWS Publications: Bangalore, India, 1990.
65. Singh, L.K.; Jha, M.K.; Chowdary, V.M. Assessing the accuracy of GIS-based multi-criteria decision analysis approaches for mapping groundwater potential. *Ecol. Indic.* **2018**, *91*, 24–37. [CrossRef]
66. Hazen, A. Discussion: Dams on sand foundations. *Trans. Am. Soc. Civ. Eng.* **1911**, *73*, 190–208.
67. Todd, D.K.; Mays, L.W. *Groundwater Hydrology*, 3rd ed.; John Wiley & Sons, Inc.: New York, NY, USA, 2005; ISBN 978-0-471-05937-0.

68. Duffy, C.J.; Al-Hassan, S. Groundwater circulation in a closed desert basin: Topographic scaling and climatic forcing. *Water Resour. Res.* **1988**, *24*, 1675–1688. [CrossRef]

69. Twidale, C.R. River patterns and their meaning. *Earth Science Rev.* **2004**, *67*, 159–218. [CrossRef]

70. Charlton, R. *Fundamentals of Fluvial Geomorphology*; Routledge: New York, NY, USA, 2008; ISBN 0203371089.

71. Horton, R.E. Drainage-basin characteristics. *Eos Trans. Am. Geophys. Union* **1932**, *13*, 350–361. [CrossRef]

72. Gelaro, R.; McCarty, W.; Suárez, M.J.; Todling, R.; Molod, A.; Takacs, L.; Randles, C.A.; Darmenov, A.; Bosilovich, M.G.; Reichle, R.; et al. The modern-era retrospective analysis for research and applications, version 2 (MERRA-2). *J. Clim.* **2017**, *30*, 5419–5454. [CrossRef]

73. Kuswanto, H.; Naufal, A. Evaluation of performance of drought prediction in Indonesia based on TRMM and MERRA-2 using machine learning methods. *MethodsX* **2019**, *6*, 1238–1251. [CrossRef]

74. Reichle, R.H.; Liu, Q.; Koster, R.D.; Draper, C.S.; Mahanama, S.P.P.; Partyka, G.S. Land surface precipitation in MERRA-2. *J. Clim.* **2017**, *30*, 1643–1664. [CrossRef]

75. Europe's eyes on Earth. The Copernicus Global Land Service (CGLS). Available online: https://land.copernicus.eu/global/ (accessed on 19 September 2022).

76. Hung, L.Q.; Batelaan, O.; De Smedt, F. Lineament extraction and analysis, comparison of LANDSAT ETM and ASTER imagery. Case study: Suoimuoi Tropical Karst Catchment, Vietnam. *Remote Sens. Environ. Monit. GIS Appl. Geol. V* **2005**, *5983*, 59830T. [CrossRef]

77. Magowe, M.; Carr, J.R. Relationship between lineaments and ground water occurrence in Western Botswana. *Groundwater* **1999**, *37*, 282–286. [CrossRef]

78. Al-Ruzouq, R.; Shanableh, A.; Yilmaz, A.G.; Idris, A.E.; Mukherjee, S.; Khalil, M.A.; Gibril, M.B.A. Dam site suitability mapping and analysis using an integrated GIS and machine learning approach. *Water* **2019**, *11*, 1880. [CrossRef]

79. Edet, A.E.; Okereke, C.S.; Teme, S.C.; Esu, E.O. Application of remote-sensing data to groundwater exploration: A case study of the Cross River State, Southeastern Nigeria. *Hydrogeol. J.* **1998**, *6*, 394–404. [CrossRef]

80. Jasrotia, A.S.; Kumar, A.; Singh, R. Integrated remote sensing and GIS approach for delineation of groundwater potential zones using aquifer parameters in Devak and Rui Watershed of Jammu and Kashmir, India. *Arab. J. Geosci.* **2016**, *9*, 1–15. [CrossRef]

81. Martin, S.L.; Hayes, D.B.; Kendall, A.D.; Hyndman, D.W. The land-use legacy effect: Towards a mechanistic understanding of time-lagged water quality responses to land use/cover. *Sci. Total Environ.* **2017**, *579*, 1794–1803. [CrossRef] [PubMed]

82. Lerner, D.N.; Harris, B. The relationship between land use and groundwater resources and quality. *Land Use Policy* **2009**, *26*, 265–273. [CrossRef]

83. Collin, M.L.; Melloul, A.J. Combined land-use and environmental factors for sustainable groundwater management. *Urban Water* **2001**, *3*, 229–237. [CrossRef]

84. Machiwal, D.; Jha, M.K.; Mal, B.C. Assessment of groundwater potential in a semi-arid region of India using remote sensing, GIS and MCDM techniques. *Water Resour. Manag.* **2011**, *25*, 1359–1386. [CrossRef]

85. Adeyeye, O.A.; Ikpokonte, E.A.; Arabi, S.A. GIS-based groundwater potential mapping within Dengi Area, North Central Nigeria. *Egypt. J. Remote Sens. Sp. Sci.* **2019**, *22*, 175–181. [CrossRef]

86. Mohallel, S.A.; Abdella, H.F.; Habibah, A.Z. Hydrogeochemical assessment of groundwater quality at Wadi Abbadi, Southern Part of Eastern Desert, Egypt. *Curr. Sci. Int.* **2019**, *8*, 422–438.

87. Ezz, H.; Gomaah, M.; Abdelwares, M. Watershed delineation and estimation of groundwater recharge for Ras Gharib Region, Egypt. *J. Geosci. Environ. Prot.* **2019**, *07*, 202–213. [CrossRef]

88. Adeyemo, J.; Olofintoye, O.O. Optimized Fourier approximation models for estimating monthly streamflow in the Vanderkloof Dam, South Africa. In *Advances in Intelligent Systems and Computing*; Springer International Publishing: Cham, Switzerland, 2014; Volume 288, pp. 293–306. ISBN 978-3-319-07493-1.

89. Swain, S.; Taloor, A.K.; Dhal, L.; Sahoo, S.; Al-Ansari, N. Impact of climate change on groundwater hydrology: A comprehensive review and current status of the Indian hydrogeology. *Appl. Water Sci.* **2022**, *12*, 1–25. [CrossRef]

90. Hassan, W.H.; Hussein, H.H.; Nile, B.K. The effect of climate change on groundwater recharge in unconfined aquifers in the western desert of Iraq. *Groundw. Sustain. Dev.* **2022**, *16*, 100700. [CrossRef]

91. Folk, R.L. *Petrologie of Sedimentary Rocks*; Hemphill Publishing Co.: Austin, TX, USA, 1974; ISBN 0-914696-14-9.